

GASEOUS STRUCTURES IN BARRED GALAXIES: EFFECTS OF THE BAR STRENGTH

WOONG-TAE KIM, WOO-YOUNG SEO, & YONGHWI KIM

Center for the Exploration of the Origin of the Universe (CEOU), Astronomy Program, Department of Physics & Astronomy, Seoul
 National University, Seoul 151-742, Republic of Korea and
 FPRD, Department of Physics & Astronomy, Seoul National University, Seoul 151-742, Republic of Korea

Accepted for publication in the ApJ

ABSTRACT

Using hydrodynamic simulations, we investigate the physical properties of gaseous substructures in barred galaxies and their relationships with the bar strength. The gaseous medium is assumed to be isothermal and unmagnetized. The bar potential is modeled as a Ferrers prolate with index n . To explore situations with differing bar strength, we vary the bar mass f_{bar} relative to the spheroidal component as well as its aspect ratio \mathcal{R} . We derive expressions as functions of f_{bar} and \mathcal{R} for the bar strength Q_b and the radius $r(Q_b)$ where the maximum bar torque occurs. When applied to observations, these expressions suggest that bars in real galaxies are most likely to have $f_{\text{bar}} \sim 0.25$ – 0.50 and $n \lesssim 1$. Dust lanes approximately follow one of x_1 -orbits and tend to be more straight under a stronger and more elongated bar, but are insensitive to the presence of self-gravity. A nuclear ring of a conventional x_2 type forms only when the bar is not so massive or elongated. The radius of an x_2 -type ring is generally smaller than the inner Lindblad resonance, decreases systematically with increasing Q_b , and slightly larger when self-gravity is included. This evidences that the ring position is not determined by the resonance but by the amount of angular momentum loss at dust-lane shocks. Nuclear spirals exist only when the ring is of the x_2 -type and sufficiently large in size. Unlike the other features, nuclear spirals are transient in that they start out as being tightly-wound and weak, and then due to the nonlinear effect unwind and become stronger until turning into shocks, with an unwinding rate higher for larger Q_b . The mass inflow rate to the galaxy center is found to be less than $0.01 M_\odot \text{ yr}^{-1}$ for models with $Q_b \lesssim 0.2$, while becoming larger than $0.1 M_\odot \text{ yr}^{-1}$ when $Q_b \gtrsim 0.2$ and self-gravity is included.

Subject headings: hydrodynamics — galaxies: ISM — galaxies: kinematics and dynamics — galaxies: nuclei — galaxies: spiral — galaxies: starburst — galaxies: structure — ISM: kinematics and dynamics — shock waves

1. INTRODUCTION

The inner parts of barred galaxies contain interesting gaseous substructures that include dust lanes, nuclear rings, and nuclear spirals (e.g., Sanders & Huntley 1976; Sakamoto et al. 1999; Knapen et al. 2002; Martini et al. 2003a,b; Sheth et al. 2005; Prieto et al. 2005; Martinez-Valpuesta et al. 2006; Comerón et al. 2009, 2010; Mazzuca et al. 2011; Hsieh et al. 2011). These substructures are thought to form as a result of gas redistribution in galaxies initiated by non-axisymmetric bar torque (e.g., Combes & Gerin 1985; Buta 1986; Shlosman et al. 1990; Garcia-Barreto et al. 1991; Buta & Combes 1996; Combes 2001). Understanding their formation and evolution is therefore of crucial importance to understand how the interstellar gas in barred galaxies is driven inward to affect star formation activities in the nuclear regions and potentially fueling of active galactic nuclei (AGN). Since their spatial locations and shapes are likely to be determined by the bar strength as well as the underlying rotation curve (e.g., Athanassoula 1992b; Peebles & Martini 2006; Comerón et al. 2009, 2010), they may also be used to probe the mass distributions in barred galaxies that are not directly observable.

While the bar substructures have been observed for a long time (e.g., Pease 1917; Sandage 1961), it is during recent years that high-quality data on their physical

properties have been compiled and compared with bar characteristics (e.g., Knapen et al. 2002; Peebles & Martini 2006; Mazzuca et al. 2008; Comerón et al. 2009, 2010; Mazzuca et al. 2011). There is increasing observational evidence that the shape and size of the bar substructures are determined primarily by the bar strength Q_b . For instance, Knapen et al. (2002) measured the curvature angles $\Delta\alpha$ of dust lanes for a sample of 9 barred spiral galaxies, and found that stronger bars favor more straight dust lanes, confirming a theoretical prediction of Athanassoula (1992b). By extending the sample size to 55 galaxies, Comerón et al. (2009) confirmed the results of Knapen et al. (2002), although they also found that a large scatter in the fit of the $\Delta\alpha$ – Q_b relationship can be reduced if the bar ellipticity is also considered in the fit. More recently, Comerón et al. (2010) measured the sizes and shapes of nuclear rings in a sample of 107 galaxies, finding that ‘stronger bars host smaller rings’ and that the ring ellipticity is in the range of 0–0.4. Mazzuca et al. (2011) reported from the analysis of 13 nuclear rings that the ring size is well correlated with the compactness of the galaxy mass distribution such that higher mass concentration implies a smaller ring. On the other hand, by analyzing dust morphology in the nuclear regions of 75 galaxies, Peebles & Martini (2006) found that tightly-wound nuclear spirals are preferentially found in galaxies with a weak bar.

On the theoretical side, the formation and evolution

of bar substructure has been extensively studied using numerical simulations on hydrodynamical models (e.g. Sanders & Huntley 1976; Roberts et al. 1979; van Albada & Roberts 1981; Athanassoula 1992b; Piner et al. 1995; Englmaier & Gerhard 1997; Patsis & Athanassoula 2000; Maciejewski et al. 2002; Maciejewski 2004a,b; Regan & Teuben 2003, 2004; Ann & Thakur 2005; Lin et al. 2008; Thakur et al. 2009) and magnetized models (e.g., Kulesza-Żydzik et al. 2009, 2010; Kulpa-Dybelet et al. 2011; Kim & Stone 2012). In particular, Athanassoula (1992b) confirmed the early notion of Prendergast (1962) that dust lanes are shocks in the gas flows. She also showed that dust lanes are more straight when the bar potential is stronger. Due to lack of numerical resolution and/or large numerical viscosity, however, early numerical works published before the middle of 1990s were unable to capture the formation of nuclear rings and spirals accurately. Piner et al. (1995) was the first who focused on the ring formation using a grid-based code with negligible numerical viscosity. Unfortunately, however, their numerical results were, at least quantitatively, contaminated by a trivial sign error in the evaluation of the bar forces, as identified by Kim et al. (2012). More recently, Ann & Thakur (2005) and Thakur et al. (2009) used SPH simulations to study gas dynamics in the central regions of barred galaxies, but they were unable to resolve nuclear spirals because most particles in their simulations are captured into a ring, leaving only a small number of particles inside the ring.

Very recently, Kim et al. (2012, hereafter Paper I) corrected the error in Piner et al. (1995) and revisited the issue of the bar-substructure formation using high-resolution simulations by varying the gas sound speed c_s and the mass of a central black hole (BH). Paper I found that the corrected bar force naturally allows the development of nuclear spirals inside a ring, which was unseen in Piner et al. (1995). In addition, Paper I showed that the ring size and the mass inflow rate \dot{M} toward the galaxy center depend rather sensitively on c_s . In models with small c_s , the rings are narrow and located away from the center. This prevents further inflows of the gas to the central regions, making \dot{M} smaller than $10^{-4} M_\odot \text{ yr}^{-1}$. On the other hand, models with large c_s have a small and broad ring, resulting in $\dot{M} \gtrsim 10^{-2} M_\odot \text{ yr}^{-1}$. Paper I further confirmed that the prediction of Buta & Combes (1996) that the shape of nuclear spirals depend on the sign of the $d(\Omega - \kappa/2)/dr$ curve such that they are trailing (leading) where $d(\Omega - \kappa/2)/dr$ is negative (positive). This suggests that nuclear spirals, if exist, are likely to be trailing in galaxies with supermassive BHs.

Since the models studied in Paper I were restricted to a particular set of the bar parameters, namely, with the bar mass $\sim 30\%$ of the spheroidal component (i.e., bulge plus bar) and the aspect ratio $\mathcal{R} = 2.5$, they were unable to study the variations in the size and shape of bar substructures with differing bar strength. In addition, the models in Paper I are all non-self-gravitating, so that the effects of self-gravity on bar substructures have yet to be explored. Although Athanassoula (1992b) considered diverse bar models with different aspect ratio and bar quadrupole moment Q_m , her models were unable to resolve nuclear rings and spirals due to insufficient resolution. While Regan & Teuben (2003, 2004) also ran a

large number of numerical simulations with varying Q_m and \mathcal{R} , their numerical results were compromised by the incorrect bar forces of Piner et al. (1995), as mentioned above.

In this paper, we present the results of a series of hydrodynamic simulations to investigate the properties of bar substructures that form. This work extends Paper I in two ways: (1) by considering various bar models with differing mass and aspect ratio and (2) by including gaseous self-gravity, while fixing the sound speed and the BH mass. We measure the curvatures of dust lanes, sizes of nuclear ring, shapes of nuclear spirals, and mass inflow rates in simulations, and study their relationships with the bar parameters. Our main objective is to explore the parametric dependence of the properties of bar substructures on the bar strength and self-gravity. This will allow us to provide physical explanations for the formation of bar substructures especially for nuclear rings and spirals, which was previously uncertain. We also compare our numerical results with observations of barred-spiral galaxies that are currently available.

Our models with varying bar strength are useful to address an important question as to what determines the position of nuclear rings. Observations indicate that nuclear rings are typically located near the inner Lindblad resonance (ILR) when there is a single ILR, or between the ILRs when there are two ILRs (e.g., Combes & Gerin 1985; Knapen et al. 1995; Comerón et al. 2010). This has often been interpreted as an indication that nuclear rings form as a consequence of the resonant interactions of the gas with the ILRs (Combes 1996; Buta & Combes 1996; see also Regan & Teuben 2003). This idea was motivated by the notion that the bar torque changes its sign whenever crossing each ILR such that in the case of a single ILR, for example, the gas inside (outside) the ILR receives a positive (negative) torque and thus moves outward (inward). This idea of the resonance-driven ring formation requires that the bar torque dominates thermal and ram pressures of the gas in governing the gas motions both inside and outside the ILR. It is clear that the bar torque dominates outside the ILR, inducing dust-lane shocks and initiating radial gas inflows. However, it is uncertain if that is also the case inside the ILR. The bar potential becomes increasingly axisymmetric toward the galaxy center, while the inflowing gas usually has large momentum and is thus unlikely to stall at the ILR. By measuring the ring positions and comparing them with the ILR radii in our models, we directly test whether the ILR is really responsible for the formation of nuclear rings.

This paper is organized as follows: In Section 2, we describe our model parameters and numerical methods. In Section 3, we define and evaluate the bar strength Q_b of our galaxy models as well as the radius $r(Q_b)$ where the maximum bar torque occurs. We provide algebraic expressions for Q_b and $r(Q_b)$ for various bar models. In Section 4, we quantify the properties of bar substructures and explore their correlations with the bar strength. We also measure the mass inflows rates. Finally, in Section 5, we summarize our results and discuss them in comparison with observations.

2. MODEL

We study gas responses to an imposed non-axisymmetric bar potential using hydrodynamic simulations with and without self-gravity, focusing on the effects of the bar strength on gaseous structures that form. We consider an initially-uniform, rotating gaseous disk with surface density $\Sigma_0 = 10 \text{ M}_\odot \text{ pc}^{-2}$. We assume that the disk is infinitesimally thin, isothermal, and unmagnetized. The simulations setups and numerical methods are identical to those in Paper I, except that some models in the present work include self-gravitational potential of the gas. Here we briefly summarize our numerical models and highlight the differences between the current models and those studied in Paper I.

The gaseous disk is placed under the external gravitational potential Φ_{ext} consisting of four components: a stellar disk, a stellar bulge, a non-axisymmetric stellar bar, and a central BH. The stellar disk is modeled by a Kuzmin-Toomre profile, the bulge by a modified Hubble profile, and the BH by a Plummer profile with mass M_{BH} . For the bar potential Φ_{bar} , we use Ferrers (1887) prolate spheroids with volume density

$$\rho = \begin{cases} \rho_{\text{bar}} (1 - g^2)^n, & \text{for } g < 1, \\ 0, & \text{elsewhere,} \end{cases} \quad (1)$$

where ρ_{bar} is the central density, $g^2 \equiv y^2/a^2 + (x^2 + z^2)/b^2$, and a and b ($\leq a$) denote the semimajor and semiminor axes of the bar, respectively. The index n represents the degree of central density concentration. Appendix presents an analytic expression of Φ_{bar} at $z = 0$ and $g < 1$ for $n = 1$.

The total mass of the bar is given by $M_{\text{bar}} = 2^{2n+3} \pi a b^2 \rho_{\text{bar}} \Gamma(n+1) \Gamma(n+2) / \Gamma(2n+4)$ (e.g., Athanassoula et al. 2009), which we control using a dimensionless parameter

$$f_{\text{bar}} = \frac{M_{\text{bar}}}{M_{\text{bar}} + M_{\text{bul}}}, \quad (2)$$

where M_{bul} denotes the bulge mass inside $r = 10 \text{ kpc}$. In our models, the total mass of the spheroidal component within 10 kpc is fixed to $M_{\text{bar}} + M_{\text{bul}} = 4.87 \times 10^{10} \text{ M}_\odot$, so that larger f_{bar} implies a less massive bulge. Another independent parameter that characterizes the bar potential is the aspect ratio $\mathcal{R} \equiv a/b$. One may also use the bar quadrupole moment $Q_m = M_{\text{bar}}(a^2 - b^2)/(5 + 2n)$ as a measure of the bar mass (e.g., Athanassoula 1992b; Regan & Teuben 2003, 2004), although we prefer f_{bar} since Q_m depends also on \mathcal{R} . The rotation curve in the bar regions is slightly changed by varying f_{bar} and \mathcal{R} , but its flat part has $v_0 = 200 \text{ km s}^{-1}$ regardless of f_{bar} and \mathcal{R} , corresponding to normal disk galaxies.

Since the parameter space is very large, Paper I fixed the bar parameters to $f_{\text{bar}} = 0.3$, $a = 5 \text{ kpc}$, and $b = 2 \text{ kpc}$, and varied c_s from 5 to 20 km s^{-1} and M_{BH} from 0 to $4 \times 10^8 \text{ M}_\odot$ to explore how gas flows change with the gas sound speed and the BH mass. In this work, we instead fix $c_s = 10 \text{ km s}^{-1}$ and $M_{\text{BH}} = 4 \times 10^7 \text{ M}_\odot$, and consider 40 models with differing $f_{\text{bar}} = 0.08$ to 0.6 and $\mathcal{R} = 1.5$ to 3.5 . Since the bar semimajor axis is fixed to $a = 5 \text{ kpc}$ in all of our models, the latter is equivalent to varying b from 3.33 to 1.43 kpc . Other parameters such as the bar pattern speed $\Omega_b = 33 \text{ km s}^{-1} \text{ kpc}^{-1}$ and the total disk mass $M_{\text{disk}} = 2.2 \times 10^{11} \text{ M}_\odot$ remain the same as in Paper I. Columns (1) – (3) of Tables

1 and 2 list the model names and parameters for non-self-gravitating and self-gravitating models, respectively. The postfixes N and G stand for no self-gravity and with self-gravity, respectively. In what follows, a model name without any postfix refers to both self-gravitating and non-self-gravitating models. Note that Model M30R25N is identical to Model cs10bh7 studied in Paper I except for the size of the inner boundary (see below).

With $\Omega_b = 33 \text{ km s}^{-1} \text{ kpc}^{-1}$, all the models have the corotation resonance at $r_{\text{CR}} = 6 \text{ kpc}$, independent of f_{bar} and \mathcal{R} . The presence of a central BH makes the rotation curve rise steeply toward the center as $\propto (M_{\text{BH}}/r)^{1/2}$, giving rise to a single ILR where $\Omega_b = \Omega - \kappa/2$. Here, Ω and κ refer to the angular and epicycle frequencies, respectively, averaged between on the major and minor axes of the bar. Unlike r_{CR} , the ILR position r_{ILR} depends slightly on f_{bar} and \mathcal{R} . Column (4) of Tables 1 and 2 gives r_{ILR} in each model. Since the bulge potential is more centrally concentrated than the bar potential, models with larger f_{bar} tend to have a smaller rotational velocity in the central regions and hence smaller r_{ILR} . For fixed f_{bar} , a larger value of \mathcal{R} corresponds to larger ρ_{bar} and thus slightly larger r_{ILR} .

For models in which self-gravity is included, we employ the method used by Shetty & Ostriker (2008) to calculate the gravitational potential from the perturbed gas surface density, $\Sigma - \Sigma_0$.¹ This method is based on Kalnajs (1971)'s scheme that is efficient on a logarithmically-spaced radial grid. As a softening parameter, we take $H/r = 0.1$ that allows for non-zero thickness of the disk in the potential calculation. In our models, the gaseous disk initially has a Toomre stability parameter of

$$Q_T \equiv \frac{\kappa c_s}{\pi G \Sigma} \approx 2.1 \left(\frac{r}{10 \text{ kpc}} \right)^{-1} \left(\frac{\Sigma}{10 \text{ M}_\odot \text{ pc}^{-2}} \right)^{-1}, \quad (3)$$

so that it is gravitationally stable. However, nuclear rings that form at around $r \sim 1 \text{ kpc}$ would achieve sufficient density to be unstable when the bar is strong.

We solve the basic equations of ideal hydrodynamics using the CMHOG code in a frame corotating with the bar (Paper I). CMHOG is third-order accurate in space and has very little numerical diffusion (Piner et al. 1995). We resolve the central regions with high accuracy by setting up a logarithmically-spaced cylindrical grid extending from 0.04 kpc at the inner boundary to 16 kpc at the outer boundary. The size of the inner boundary taken in the present models is twice larger than that in Paper I: we checked that this makes negligible differences in the properties of bar substructures except for the mass inflow rate across the inner boundary that becomes larger, by $\sim 10\%$ on average, in the current models. The number of zones in our models is 1024 in the radial direction and 535 in the azimuthal direction that covers the half-plane. The corresponding spatial resolution is $\Delta r = 0.23, 5.86$, and 93.8 pc at the inner boundary, $r = 1 \text{ kpc}$, and the outer boundary, respectively. We adopt the outflow and continuous boundary conditions at the inner and outer boundaries, respectively, while

¹ In our self-gravitating models, gravity of the initial gaseous disk with surface density Σ_0 is neglected in order to make the initial rotation curve identical to that in the non-self-gravitating counterparts.

Table 1
Model Parameters and Curvatures of Dust Lanes in Non-self-gravitating Models

Model	f_{bar}	\mathcal{R}	r_{ILR} (kpc)	Q_b	$r(Q_b)$ (kpc)	α_1 (deg)	α_2 (deg)	$\Delta\alpha$ (deg)
(1)	(2)	(3)	(4)	(5)	(6)	(7)	(8)	(9)
M08R15N	0.08	1.5	2.2	0.02	3.60	70.5 ± 0.5	35.8 ± 0.9	64.2 ± 2.5
M08R20N	0.08	2.0	2.2	0.05	3.30	74.4 ± 5.8	35.8 ± 2.9	63.4 ± 12.6
M08R25N	0.08	2.5	2.2	0.07	3.12	74.1 ± 2.6	44.2 ± 2.3	46.3 ± 3.4
M08R30N	0.08	3.0	2.2	0.09	3.04	72.8 ± 3.0	53.3 ± 4.0	30.1 ± 6.6
M08R35N	0.08	3.5	2.2	0.12	2.98	74.3 ± 1.7	59.6 ± 5.2	22.2 ± 6.7
M15R15N	0.15	1.5	2.1	0.04	3.58	75.1 ± 1.4	34.5 ± 1.6	81.6 ± 2.9
M15R20N	0.15	2.0	2.1	0.08	3.28	71.7 ± 3.2	49.6 ± 4.3	36.3 ± 9.0
M15R25N	0.15	2.5	2.2	0.13	3.12	75.3 ± 2.5	63.4 ± 2.3	19.6 ± 4.2
M15R30N	0.15	3.0	2.2	0.17	3.04	73.4 ± 2.5	68.3 ± 2.4	8.2 ± 4.4
M15R35N	0.15	3.5	2.2	0.21	2.98	74.3 ± 5.1	71.1 ± 5.4	5.0 ± 3.6
M30R15N	0.30	1.5	1.8	0.08	3.56	70.7 ± 3.4	38.9 ± 3.9	63.4 ± 10.0
M30R20N	0.30	2.0	1.8	0.16	3.26	78.8 ± 3.1	60.6 ± 4.5	33.4 ± 9.6
M30R25N	0.30	2.5	2.1	0.23	3.10	79.8 ± 1.5	68.5 ± 1.4	16.8 ± 2.8
M30R30N	0.30	3.0	2.1	0.31	3.02	78.4 ± 2.8	75.1 ± 0.9	4.7 ± 3.9
M30R35N	0.30	3.5	2.1	0.39	2.90	80.8 ± 0.3	79.3 ± 0.5	2.2 ± 0.2
M60R15N	0.60	1.5	1.4	0.14	3.42	81.0 ± 3.3	52.6 ± 11.1	53.4 ± 23.1
M60R20N	0.60	2.0	1.3	0.28	3.18	79.2 ± 3.1	70.7 ± 1.1	12.8 ± 5.7
M60R25N	0.60	2.5	1.3	0.41	3.02	79.3 ± 3.4	74.8 ± 1.9	6.9 ± 5.0
M60R30N	0.60	3.0	1.9	0.54	2.92
M60R35N	0.60	3.5	1.9	0.67	2.88

Note. — f_{bar} is the fraction of the bar mass relative to the spheroidal component (bar plus bulge); \mathcal{R} is the ratio of the bar semimajor axis to the semiminor axis; r_{ILR} is the radius of the ILR; Q_b is the bar strength defined by equation (4); $r(Q_b)$ is the radius of the maximum bar torque; α_1 and α_2 are the tangent angles to a dust-lane segment at the inner and outer ends relative to the x -axis, respectively; $\Delta\alpha$ is the dust lane curvature defined by equation (7).

Table 2
Model Parameters and Curvatures of Dust Lanes in Self-gravitating Models

Model	f_{bar}	\mathcal{R}	r_{ILR} (kpc)	Q_b	$r(Q_b)$ (kpc)	α_1 (deg)	α_2 (deg)	$\Delta\alpha$ (deg)
(1)	(2)	(3)	(4)	(5)	(6)	(7)	(8)	(9)
M08R15G	0.08	1.5	2.2	0.02	3.60	69.7 ± 1.5	37.1 ± 1.5	60.2 ± 1.8
M08R20G	0.08	2.0	2.2	0.05	3.30	72.1 ± 7.6	35.8 ± 2.6	57.1 ± 15.0
M08R25G	0.08	2.5	2.2	0.07	3.12	70.7 ± 3.8	47.2 ± 10.1	39.9 ± 20.8
M08R30G	0.08	3.0	2.2	0.09	3.04	69.5 ± 2.1	52.6 ± 2.7	25.5 ± 5.4
M08R35G	0.08	3.5	2.2	0.12	2.98	73.6 ± 4.5	61.4 ± 6.7	28.9 ± 5.3
M15R15G	0.15	1.5	2.1	0.04	3.58	74.2 ± 4.0	39.1 ± 1.5	74.7 ± 13.9
M15R20G	0.15	2.0	2.1	0.08	3.28	71.0 ± 4.4	50.3 ± 4.7	32.8 ± 13.2
M15R25G	0.15	2.5	2.2	0.13	3.12	75.0 ± 3.5	65.6 ± 2.3	16.1 ± 4.4
M15R30G	0.15	3.0	2.2	0.17	3.04	72.9 ± 0.9	69.0 ± 3.0	6.3 ± 4.1
M15R35G	0.15	3.5	2.2	0.21	2.98	74.7 ± 1.6	69.8 ± 3.5	8.0 ± 6.8
M30R15G	0.30	1.5	1.8	0.08	3.56	74.5 ± 4.2	42.7 ± 3.6	65.7 ± 19.8
M30R20G	0.30	2.0	1.8	0.16	3.26	75.1 ± 5.9	60.6 ± 4.9	25.2 ± 11.1
M30R25G	0.30	2.5	2.1	0.23	3.10	78.5 ± 2.6	69.7 ± 2.8	18.2 ± 10.6
M30R30G	0.30	3.0	2.1	0.31	3.02	78.2 ± 3.2	75.2 ± 5.0	6.4 ± 6.0
M30R35G	0.30	3.5	2.1	0.39	2.90	79.6 ± 0.1	79.7 ± 0.5	2.7 ± 1.2
M60R15G	0.60	1.5	1.4	0.14	3.42	80.2 ± 3.1	57.1 ± 5.7	64.2 ± 24.0
M60R20G	0.60	2.0	1.3	0.28	3.18	79.1 ± 4.1	69.3 ± 8.9	22.8 ± 16.2
M60R25G	0.60	2.5	1.3	0.41	3.02	76.6 ± 3.2	72.7 ± 1.5	9.2 ± 9.8
M60R30G	0.60	3.0	1.9	0.54	2.92
M60R35G	0.60	3.5	1.9	0.67	2.88

Note. — See Table 1 for the definitions of the various symbols.

taking the periodic conditions at the azimuthal boundaries. The bar potential is slowly turned on over one bar revolution time $2\pi/\Omega_b = 186$ Myr to minimize transients in the flows caused by its sudden introduction. All the models are run until 1 Gyr.

3. BAR STRENGTH

One of the key parameters that govern the gas dynamics in barred galaxies is the bar strength which depends on both f_{bar} and \mathcal{R} . In this section, we evaluate the

bar strength of our numerical models that will be used to analyze the properties of bar substructures in Section 4. We also provide fitting formulae for the bar strength and the position of the maximum bar torque for future purposes.

It has often been customary to measure the bar strength using the dimensionless parameter Q_b defined by

$$Q_b \equiv \frac{F_T(r, \phi)}{F_R(r)} \Big|_{\text{max}}, \quad (4)$$

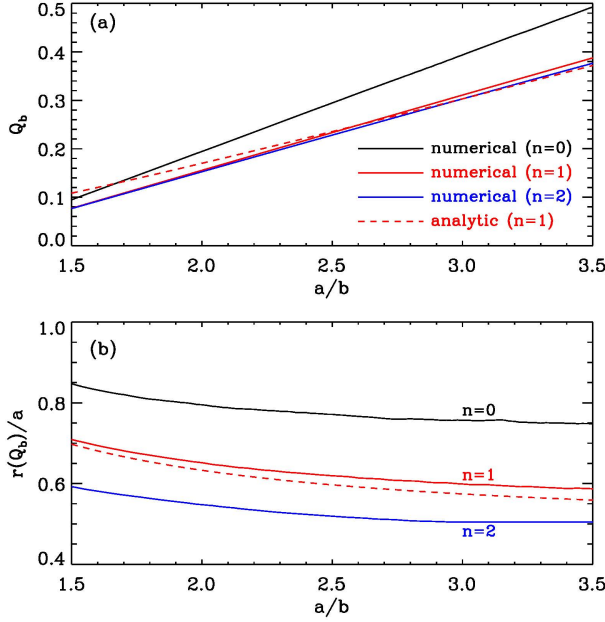


Figure 1. Dependence of the bar strength Q_b and the maximum-torque radius $r(Q_b)$ on the bar aspect ratio $\mathcal{R} = a/b$ for $f_{\text{bar}} = 0.3$. The solid curves plot the numerical results for our galaxy models with $n = 0, 1, 2$ Ferrers bars, while the dashed lines are for the analytic results assuming flat rotation.

where $F_T = -(\partial\Phi_{\text{bar}}/\partial\phi)/r$ is the tangential force due to the non-axisymmetric bar potential and $F_R = -(1/2\pi) \int_0^{2\pi} \partial\Phi_{\text{ext}}/\partial r d\phi$ is the azimuthally-averaged radial force (e.g., Combes & Sanders 1981; Laurikainen & Salo 2002; Block et al. 2004; Laurikainen et al. 2004, 2006; Peeples & Martini 2006; Comerón et al. 2009, 2010).² Physically, Q_b corresponds to the maximum bar torque applied to a gaseous material in orbital motion relative to its specific kinetic energy. Block et al. (2004) found that Q_b is deeply related to the class of barred-spiral galaxies such that SA galaxies have $Q_b \lesssim 0.1$, while $Q_b \gtrsim 0.15$ for SB galaxies.

Since the bar torque is stronger for a more massive and elongated bar, Q_b should be an increasing function of f_{bar} and \mathcal{R} . It is straightforward to calculate Q_b values of our galaxy models as well as the radius $r(Q_b)$ where $|F_T|/F_R$ is maximized. Figure 1 plots as solid lines the resulting Q_b and $r(Q_b)$ as functions of \mathcal{R} for the Ferrers bar with $f_{\text{bar}} = 0.3$ and $n = 0, 1, 2$. Note that when $f_{\text{bar}} = 0.3$, Q_b for $n = 2$ is not much different from the case with $n = 1$, while $r(Q_b)$ becomes smaller by $\sim 16\%$ as n increases from 1 to 2. Also plotted in Figure 1 as dashed lines are the analytic expressions derived in Appendix for the Ferrers bars with $n = 1$ assuming flat rotation, which agrees with the numerical results within less than 15%. The difference between the numerical and analytic results for $n = 1$ is of course due to the fact that the rotation curves in our models are not strictly flat but decrease slowly with r in the regions of the maximum bar torque, tending to increase $r(Q_b)$ compared to the case with exactly flat rotation. Columns (5) and (6) of Tables

1 and 2 list Q_b and $r(Q_b)$ of our numerical models. By varying f_{bar} , \mathcal{R} , and n , we find that

$$Q_b = \begin{cases} 0.58 f_{\text{bar}}^{0.89} (a/b - 1), & \text{for } n = 0, \\ 0.44 f_{\text{bar}}^{0.87} (a/b - 1), & \text{for } n = 1, \\ 0.38 f_{\text{bar}}^{0.79} (a/b - 1), & \text{for } n = 2, \end{cases} \quad (5)$$

and

$$\frac{r(Q_b)}{a} = \begin{cases} 1.024 - 0.161(a/b) + 0.024(a/b)^2, & \text{for } n = 0, \\ 0.934 - 0.196(a/b) + 0.028(a/b)^2, & \text{for } n = 1, \\ 0.817 - 0.197(a/b) + 0.031(a/b)^2, & \text{for } n = 2, \end{cases} \quad (6)$$

are good fits, within 5%, to the numerical results. While Q_b is linearly proportional to \mathcal{R} , $r(Q_b)$ depends very weakly on \mathcal{R} and is independent of f_{bar} . The reason for Q_b varying less steeply than $f_{\text{bar}}^{1.0}$ is that large f_{bar} increases the rotational velocity slightly near the regions where the bar torque achieves its maximum.

4. SIMULATION RESULTS

Paper I presented gas dynamical evolution of Model M30R25N with $Q_b = 0.23$ ($f_{\text{bar}} = 0.3$ and $\mathcal{R} = 2.5$) in detail. Evolution of other models with differing Q_b are qualitatively similar except that dust lanes and/or nuclear rings are absent if f_{bar} and/or \mathcal{R} are too large. In this section, we first briefly describe the main evolutionary features and the conditions for the existence of dust lanes and nuclear rings, and then present detailed analyses of the properties of bar substructures formed in our models.

4.1. Overall Morphology

As the non-axisymmetric bar potential is slowly turned on, initially-circular gas orbits are perturbed due to the bar torque, creating overdense ridges at the downstream side of the bar major axis. As the amplitude of the bar potential grows further, the ridges soon develop into dust-lane shocks. Dust-lane shocks are found unstable to the wiggle instability identified by Wada & Koda (2004) (see also Kim & Ostriker 2006) and form clumps with high vorticity (see Paper I for more detailed description). Gas loses angular momentum at the shocks, flows radially inward, and forms a nuclear ring at the position where the centrifugal force balances the external gravity. Sonic perturbations launched from the ring propagate inward and excite $m = 2$ nuclear spirals in the nuclear regions. With $M_{\text{BH}} = 7 \times 10^7 M_{\odot}$, nuclear spirals that persist in our models are all trailing.

Figures 2 and 3 display snapshots of gas surface density in logarithmic scale at $t = 0.3$ Gyr from all non-self-gravitating and self-gravitating models, respectively. Figure 4 plots density distributions at $t = 0.8$ Gyr for both non-self-gravitating (two upper rows) and self-gravitating (two bottom rows) models with $\mathcal{R} = 2.0$ and 3.0. The inner ± 5 kpc regions are shown. The bar is oriented vertically along the y -axis. The solid lines in each panel plot x_1 -orbits that cut the x -axis at $x_c = 0.8, 1.4, 2.0$, and 3.6 kpc under the total external potential. It is apparent that gas responses inside the outermost x_1 -orbit with $x_c = 3.6$ kpc are quite dramatic, while the outer regions are relatively unperturbed (e.g., Kim & Stone 2012).

At $t = 0.3$ Gyr, all the models with $Q_b < 0.5$ ($f_{\text{bar}} \leq 0.3$ or $\mathcal{R} \leq 2.5$) contain well-defined dust lanes

² The non-axisymmetric torque is sometimes represented by Q_g that includes a contribution from spiral arms (e.g., Durbala et al. 2009; Comerón et al. 2010). In our models, $Q_b = Q_g$ since no spiral arm is considered.

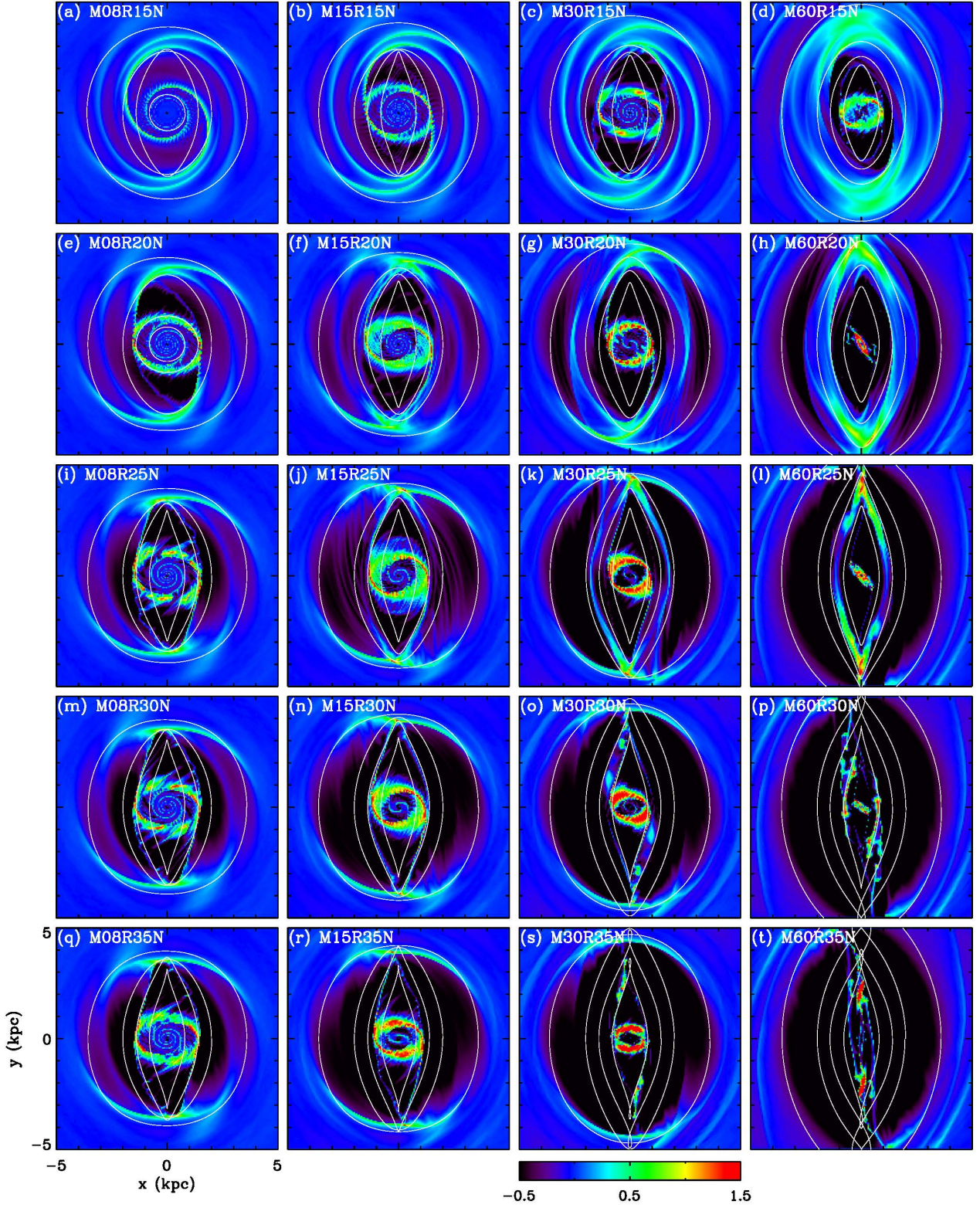


Figure 2. Logarithm of the gas surface density at $t = 0.3$ Gyr for non-self-gravitating models. Each panel shows the inner ± 5 kpc regions where the bar is oriented vertically along the y -axis. Each row corresponds to models with $\mathcal{R} = 1.5, 2.0, 2.5, 3.0,$ and 3.5 from top to bottom, while each column is for models with $f_{\text{bar}} = 0.08, 0.15, 0.3,$ and 0.6 from left to right. Solid lines in each panel draw x_1 -orbits that cut the x -axis at $x_c = 0.8, 1.4, 2.0,$ and 3.6 kpc. Color bar labels $\log(\Sigma/\Sigma_0)$.

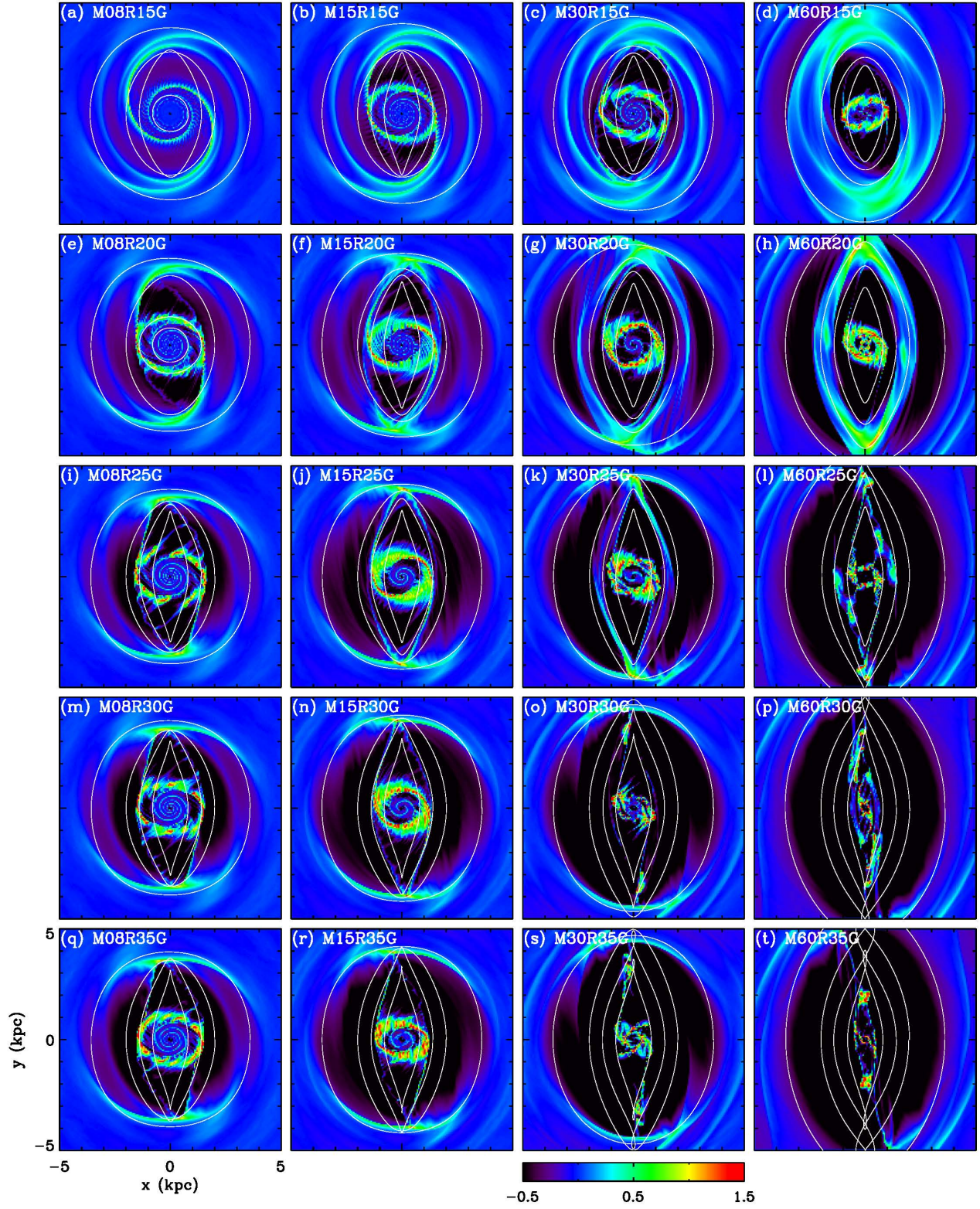


Figure 3. Same as Figure 2, but for self-gravitating models.

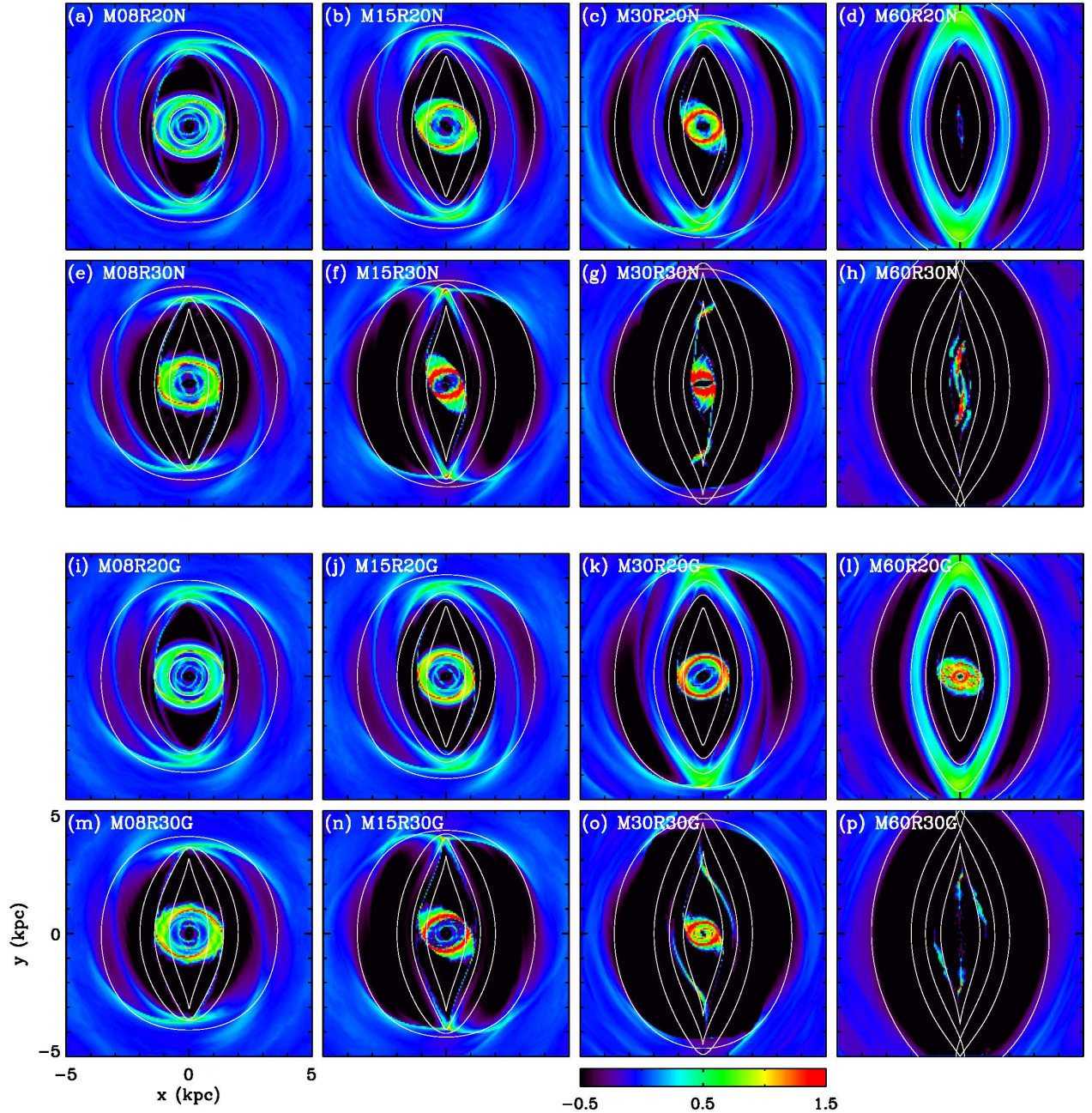


Figure 4. Logarithm of the gas surface density at $t = 0.8$ Gyr for all models with $\mathcal{R} = 2.0$ and 3.0 . The two upper rows plot the non-self-gravitating models, while the two bottom rows are for the self-gravitating models. Solid lines in each panel draw x_1 -orbits that cut the x -axis at $x_c = 0.8, 1.4, 2.0$, and 3.6 kpc. Color bar labels $\log(\Sigma/\Sigma_0)$.

that follow an x_1 -orbit reasonably well, although they become weaker at $t = 0.8$ Gyr. On the other hand, Models with $Q_b > 0.5$ do not possess features that resemble observed dust lanes. In these high- Q_b models, the bar torque is so strong that the gas inside the outermost x_1 -orbit loses most of its initial angular momentum even in the developing stage of dust lanes ($t \sim 0.13$ Gyr for Model M60R35N). With the shocked gas rapidly lost to the nuclear regions and subsequently to the inner boundary, there remains no material available to support the dust lanes in the bar regions. In these models, the bar

regions are occupied by gas blobs in a filamentary shape that are repeatedly stretched and folded on the course of orbital motions along x_1 -orbits about the center. Comparison between Figures 2 and 3 shows that the shape of dust lanes is not much affected by self-gravity.

Figures 2 also shows that conventional x_2 -type rings, that is, rings whose shape is similar to x_2 -orbits, exist when $f_{\text{bar}} \leq 0.3$ or $\mathcal{R} \leq 1.5$, in non-self-gravitating models. Rings are quite clumpy even in non-self-gravitating models due to addition of clumps produced by the wiggle instability at the dust-lane shocks. Nuclear rings in

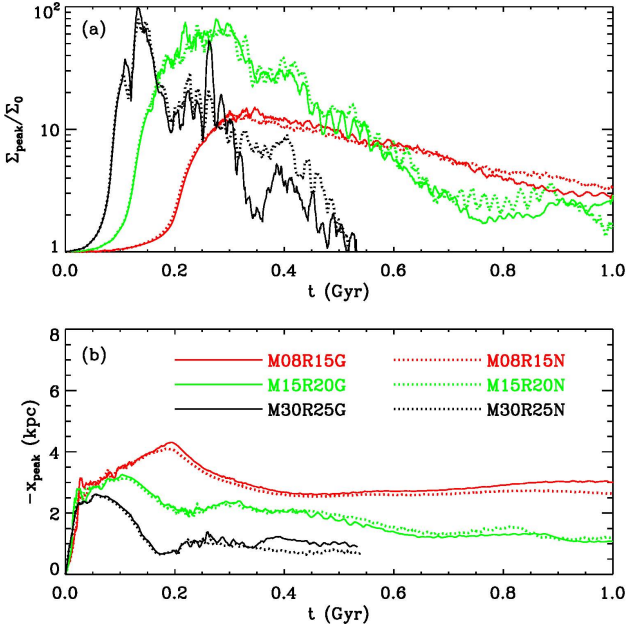


Figure 5. Temporal evolution of (a) the peak gas surface density Σ_{peak} and (b) the x -coordinate x_{peak} of the dust lanes at $r = 1.5$ kpc for Models M08R15, M15R20, and M30R25. The solid and dotted lines are for the self-gravitating and non-self-gravitating models, respectively. For Models M30R25N and M30R25G, only the results up to $t = 0.54$ Gyr are shown, after which dust lanes are too weak to be defined well.

Models M60R20N and M60R25N are highly inclined relative to the x -axis at $t = 0.3$ Gyr and gradually precess to align their long axes to the bar major axis, eventually becoming x_1 -type rings, although they become very weak at late time (e.g., Fig. 4d). In Models M60R30N and M60R35N, orbits of gas in the nuclear regions are highly transient to be considered as rings. In self-gravitating models, on the other hand, rings that form are all of the x_2 type (Fig. 3). In Models M60R30G and M60R35G, rings at $t = 0.3$ Gyr are so small that they become weaker with time by losing mass directly to the central hole, disappearing at $t \sim 0.75$ Gyr. For models that form an x_2 -type ring, rings are larger in size in self-gravitating models than in non-self-gravitating models (Fig. 4). We will explain how gas orbits are affected by the bar potential and self-gravity in Section 4.3 below.

As Q_b decreases, angular momentum loss at the shocks becomes smaller, resulting in a larger nuclear ring. Dust lanes are correspondingly located further downstream from the bar major axis since their inner ends are always attached to a nuclear ring. While dust lanes become weaker with time after the peak strength is attained, nuclear rings remain strong until the end of the runs (e.g., Fig. 4), suggesting that they are long-lived features (e.g., Allard et al. 2006; Sarzi et al. 2007; Comerón et al. 2010). In Models M08R15N and M08R15G with $Q_b = 0.02$, the bar torque is so weak that the amount of gas moving in along the dust lanes is not sufficient to form an appreciable ring until the end of the runs.

The presence of nuclear spirals is deeply related to the shape and size of a nuclear ring. There is no chance to possess nuclear spirals in models with an eccentric x_1 -type ring. Even in models with an x_2 -type ring, nuclear spirals are absent if a nuclear ring is too small (as in Mod-

els M30R35N, M30R35G, M60R20G, and M60R25G) to provide enough space for coherent structures to grow. In Models M08R15N and M08R15G, on the other hand, the inflowing gas excites trailing spiral waves at $r \sim 1$ kpc that propagate radially inward and turn into nuclear spirals. We defer the more detailed discussion on temporal evolution of nuclear spirals to Section 4.4.

4.2. Dust Lanes

To quantify the strength and displacement of dust lanes from the bar major axis, we confine to the regions with $r = 1.5$ kpc and measure the x -coordinate, x_{peak} , of the position where gas surface density is maximized at each time. Figure 5 plots the temporal changes of the peak surface density Σ_{peak} as well as x_{peak} at $r = 1.5$ kpc in Models M08R15, M15R20, and M30R25. The solid and dotted lines are for the self-gravitating and non-self-gravitating models, respectively. In Model M30R25, Σ_{peak} rises with time and peaks at $t \sim 0.13 - 0.15$ Gyr after which it decreases with time as the bar regions become increasingly evacuated due to gas infalls to the ring. At early time when the bar potential is weak, dense ridges form at $x_{\text{peak}} \sim -2.5$ kpc which move closer to the bar major axis as they turn to dust-lane shocks and stay at $x_{\text{peak}} \sim -1$ kpc. In these models with $Q_b = 0.25$, the decay of the dust lanes is relatively rapid that they become almost invisible after $t = 0.54$ Gyr. The temporal behaviors of Σ_{peak} and x_{peak} are qualitatively the same for other models with different bar strength, although the dust lanes tend to decay more slowly and locate farther from the bar major axis as Q_b decreases. Note that while the strength of dust lanes varies with time considerably, their location and shapes do not change much after $t = 0.25$ Gyr. Note also that self-gravity does not make much changes in Σ_{peak} and x_{peak} . This is because dust lanes with typical density $\Sigma_{\text{peak}} \sim 100 \text{ M}_\odot \text{ pc}^{-2}$ at $r = 1.5$ kpc have $Q_T \sim 1.4$, larger than unity (e.g., Eq. [3]). In addition, dust lanes are known to possess strong velocity shear, about 10 times larger than the velocity shear in disks at large (Paper I), which tends to reduce the mass-collecting effect of self-gravity in dust lanes.

Comerón et al. (2009) defined the dimensionless curvature of a dust-lane segment as

$$\Delta\alpha = \frac{\alpha_1 - \alpha_2}{|\mathbf{r}_1 - \mathbf{r}_2|} r(Q_b), \quad (7)$$

where $\alpha_{1,2}$ and $\mathbf{r}_{1,2}$ indicate the tangent angle to, and the position vector of, the inner and outer ends of the segment, respectively. This extends the definition of $\Delta\alpha$ in Knapen et al. (2002) to take into account the length of the host bar. To measure $\Delta\alpha$, Comerón et al. (2009) selected a constant-curvature part of a dust lane in each galaxy, with the determination of both ends relying on visual inspection. In order to obtain $\Delta\alpha$ unambiguously from our numerical models, we instead confine to a dust-lane segment bounded by the fixed position angles $\phi_{1,2} = 135^\circ, 100^\circ$ (or, $\phi_{1,2} = -45^\circ, -80^\circ$) from the positive x -axis, and measure $\alpha_{1,2}$ and $\mathbf{r}_{1,2}$ at both ends. Columns (7)–(9) of Tables 1 and 2 list the mean values (together with standard deviations) of α_1 , α_2 , and $\Delta\alpha$ averaged over $t = 0.25 - 0.35$ Gyr for models that possess dust lanes. While α_2 varies rather sensitively with Q_b , $\alpha_1 \sim 70^\circ - 80^\circ$ does not change much, indicating that $\Delta\alpha$

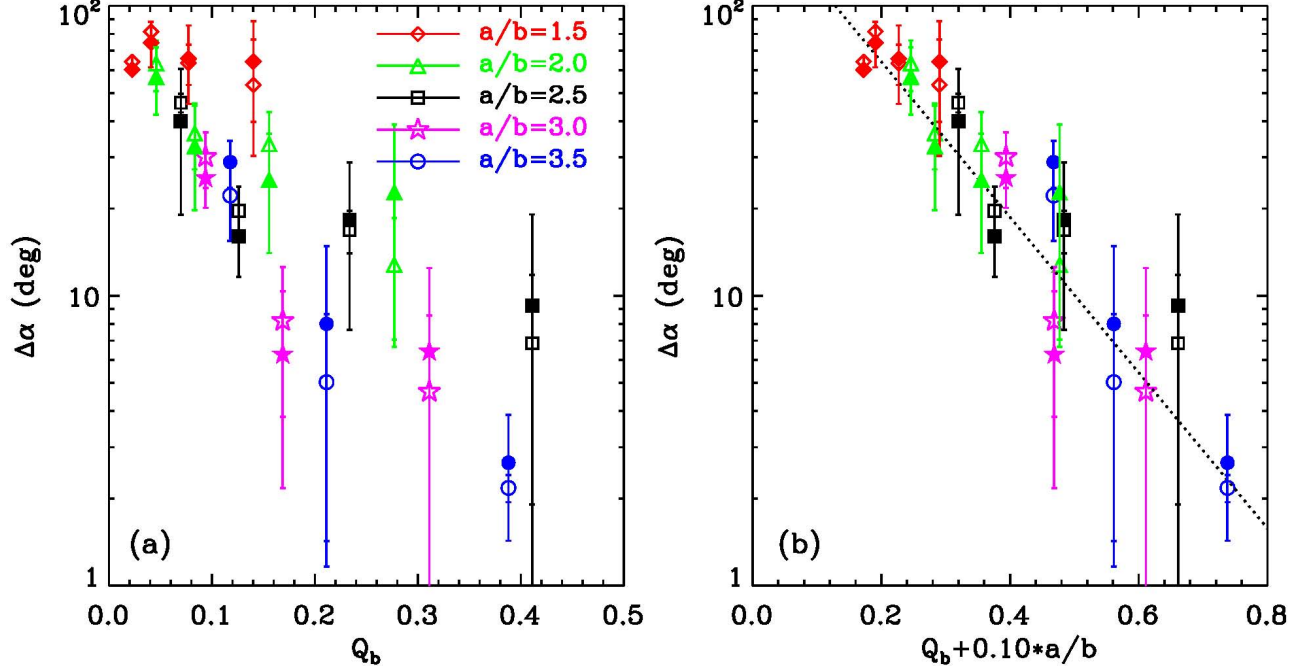


Figure 6. Curvatures $\Delta\alpha$ of dust lanes as functions of (a) Q_b alone and (b) a linear combination of Q_b and $\mathcal{R} = a/b$ for all models that possess dust lanes. Various symbols give the mean values of $\Delta\alpha$ averaged over $t = 0.25$ – 0.35 Gyr, while the errorbars indicate the standard deviations. In both panels, filled and open symbols are for self-gravitating and non-self-gravitating models, respectively. The dotted line in (b) draws the best fit, expressed in equation (8).

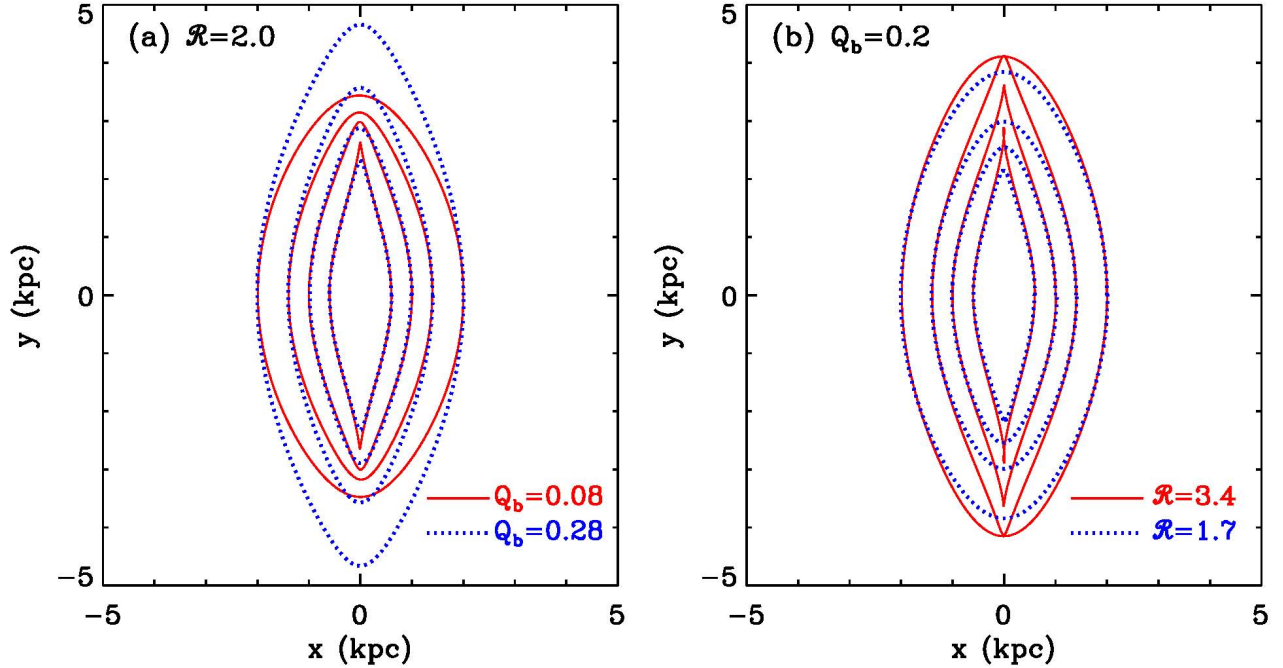


Figure 7. Dependence of x_1 -orbits with $x_c = 0.6, 1.0, 1.4, 2.0$ kpc (a) on Q_b when $\mathcal{R} = 2.0$ is fixed, and (b) on \mathcal{R} when $Q_b = 0.2$ is fixed. Note that the parts x_1 -orbits in a quadrant are more curved as x_c increases or \mathcal{R} decreases.

is determined primarily by the tangent angle at the outer end of dust lanes.

Figure 6a plots $\Delta\alpha$ measured from our numerical models as a function of Q_b . Filled and open symbols are for self-gravitating and non-self-gravitating models, respectively. These agree within error bars, indicating that self-gravity does not affect the shape of dust lanes much. In general, $\Delta\alpha$ decreases with increasing Q_b , consistent with the prediction of Athanassoula (1992b) (see also Knapen

et al. 2002). Note however that there is a considerable scatter in $\Delta\alpha$ for given Q_b . Comerón et al. (2009) found that the spread in the data points can be much reduced by fitting them using a linear combination of $\Delta\alpha$ and \mathcal{R} . We follow the same procedure and find the best fit

$$Q_b + 0.10\mathcal{R} = 0.87 - 0.37 \log \Delta\alpha, \quad (8)$$

for all models, which is plotted as a dotted line in Figure 6b. The chi-square measure of equation (8) is about 3

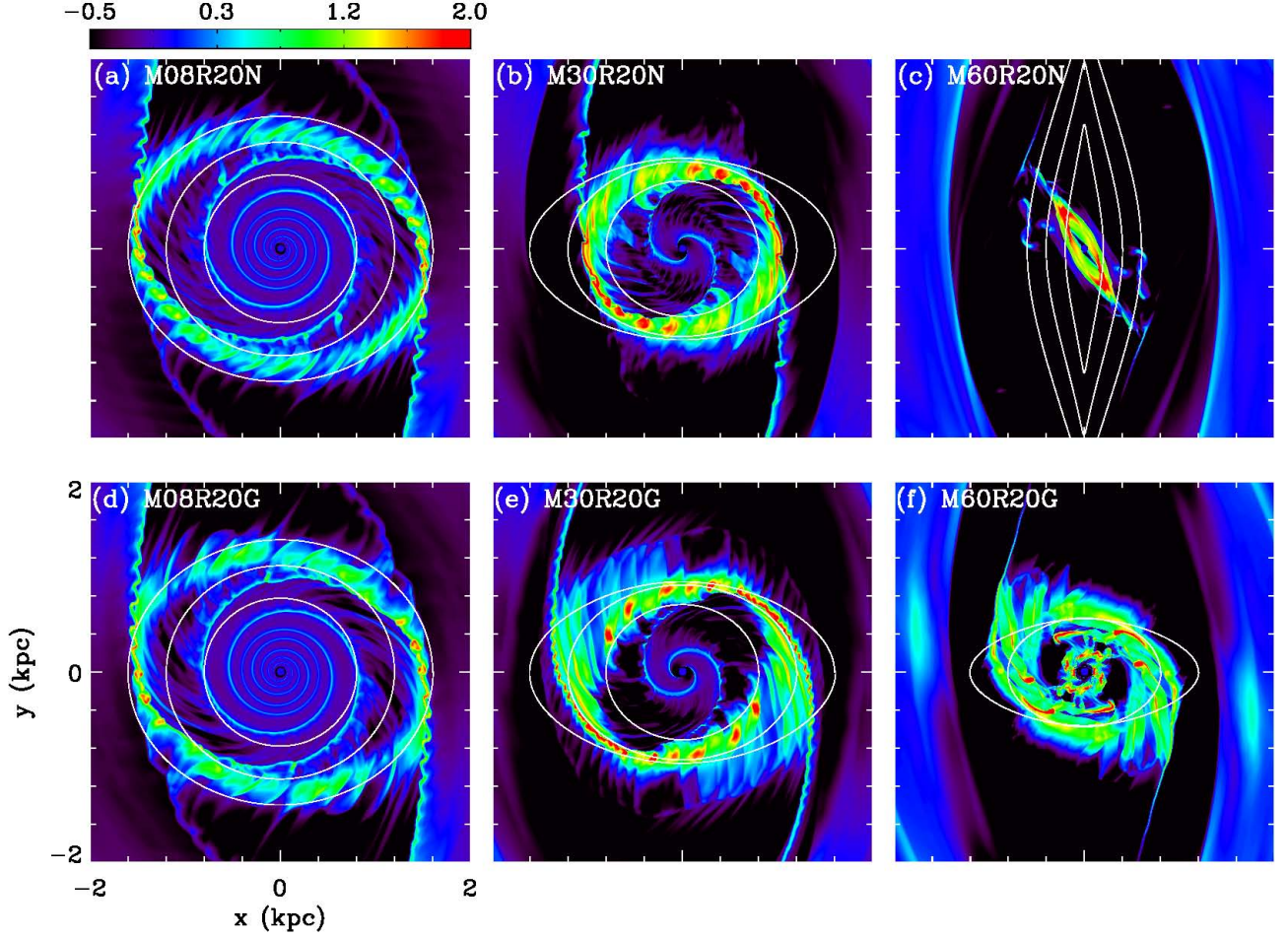


Figure 8. Snapshots of logarithm of surface density at $t = 0.3$ Gyr in the inner 2 kpc regions of non-self-gravitating models (a) M08R20N, (b) M30R20N, and (c) M60R20N, and self-gravitating models (d) M08R20G, (e) M30R20G, and (f) M60R20G. The solid lines draw x_2 -orbits that cut the x -axis at $x_c = 0.8, 1.2, 1.6$ kpc in (a), (b), (d), and (e), x_1 -orbits with $x_c = 0.2, 0.4, 0.6$ kpc in (c), and x_2 -orbits with $x_c = 0.8, 1.2$ kpc in (f). Color bar labels $\log(\Sigma/\Sigma_0)$.

times smaller than that of the best fit using only Q_b . Equation (8) implies that more elongated bars lead to more straight dust lanes.

The behavior of $\Delta\alpha$ upon Q_b and \mathcal{R} given in equation (8) can be qualitatively understood from the facts that dust lanes roughly follow x_1 -orbits and that they move closer to the bar major axis as Q_b increases. Figure 7 illustrates the changes in the shapes of x_1 -orbits with $x_c = 0.6, 1.0, 1.4, 2.0$ kpc as Q_b or \mathcal{R} varies. For fixed \mathcal{R} , the parts of x_1 -orbits, say, in the second or fourth quadrant where dust lanes are located, are clearly more curved as x_c increases, explaining larger $\Delta\alpha$ in models with smaller Q_b . For fixed Q_b , x_1 -orbits are more acute near the y -axis under a more elongated bar (i.e., larger \mathcal{R}), while they are largely independent of \mathcal{R} near the x -axis. This makes α_1 almost unchanged with \mathcal{R} , while causing α_2 to increase with \mathcal{R} , resulting in smaller $\Delta\alpha$ for larger \mathcal{R} .

4.3. Nuclear Ring

A conventional wisdom about nuclear rings is that they form near the ILRs as a result of resonant interactions of gas with the background potential (e.g., Combes 1996; Buta & Combes 1996). In this subsection, we use our numerical models to study what controls the ring for-

mation and its size when there is a single ILR. Paper I showed that the mass of a central BH (and thus the number and locations of ILRs) does not much affect the physical properties of nuclear rings that form, so that the results presented below hold also for models with two ILRs. We first describe the results of non-self-gravitating models and then discuss the effect of self-gravity on nuclear rings.

4.3.1. Non-self-gravitating Models

Inspection of Figure 2 reveals that the ring shape and its position depend on f_{bar} and/or \mathcal{R} . To show this more clearly, the upper panels of Figure 8 zoom in on the central ± 2 kpc regions and plots density distributions in logarithmic scale at $t = 0.3$ Gyr together with a few x_1 - or x_2 -orbits for selected models with $\mathcal{R} = 2.0$. It is apparent that Models M08R20N and M30R20N have an x_2 -type nuclear ring, while the ring in Model M60R20N is inclined in the galaxy plane with respect to the x -axis. Rings become smaller with increasing f_{bar} , while Model M60R20N has a very eccentric ring.

To illustrate how nuclear rings form in our models, we go back to early time when they were beginning to shape. Figure 9 plots the instantaneous streamlines of the gas that starts from Point A marked at $(x, y) =$

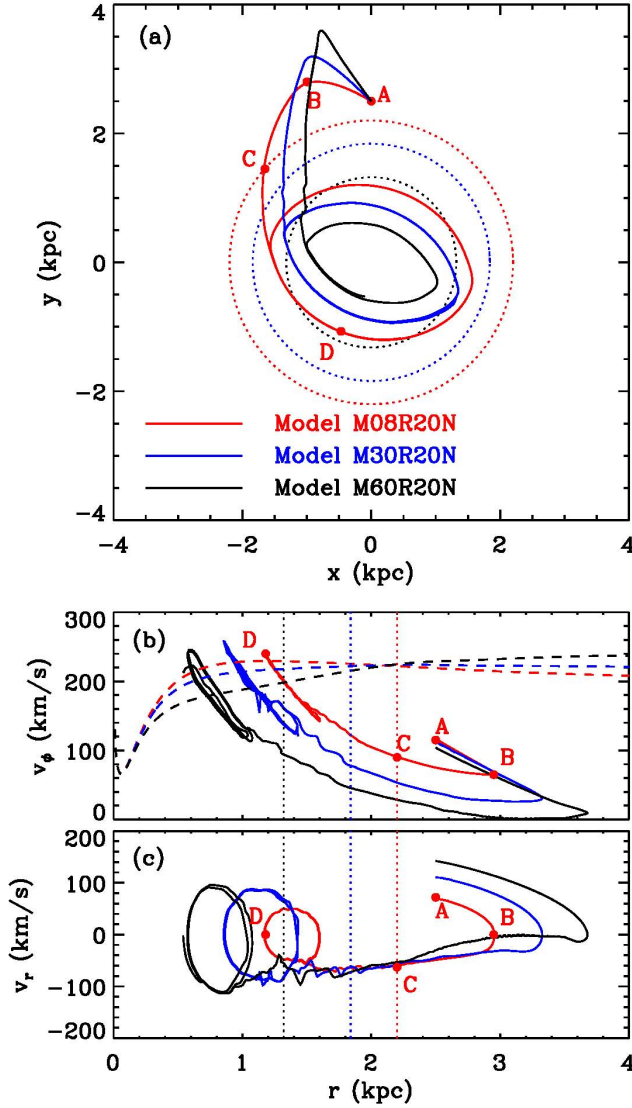


Figure 9. (a) Instantaneous streamlines of the gas that starts from Point A $(x, y) = (0, 2.5 \text{ kpc})$ in Model M08R20N at $t = 0.25 \text{ Gyr}$ (red), Model M30R20N at $t = 0.15 \text{ Gyr}$ (blue), and Model M60R20N at $t = 0.12 \text{ Gyr}$ (black) when a nuclear ring is beginning to form. The dotted circles mark the locations of the ILR at $r_{\text{ILR}} = 2.2, 1.8, 1.3 \text{ kpc}$ for Models M08R20N, M30R20N, M60R20N, respectively. (b and c) The variations of the azimuthal and radial velocities of the gas along the paths shown in (a). The ILRs are indicated as vertical lines. In (b), the dashed lines draw the equilibrium rotation curve, averaged between on the major and minor axes of the bar, in each model.

$(0, 2.5 \text{ kpc})$ as well as the variations of the rotational and azimuthal velocities in the inertial frame along the streamlines for Model M08R20N at $t = 0.25 \text{ Gyr}$ (red), Model M30R20N at $t = 0.15 \text{ Gyr}$ (blue), and Model M60R20N at $t = 0.12 \text{ Gyr}$ (black). In each panel, the dotted circles or vertical lines mark the ILR located at $r_{\text{ILR}} = 2.2, 1.8, 1.3 \text{ kpc}$ for Models M08R20N, M30R20N, M60R20N, respectively. Dashed lines in Figure 9b draw the equilibrium rotation curve, averaged between on the major and minor axes of the bar, in each model. A similar plot is given in Figure 5 of Paper I for models with no BH and in Figure 5 of Kim & Stone (2012) for magnetized models.

Outside the ILR, the bar provides a negative torque

for the gas, producing dust-lane shocks. In Model M08R20N, the gas that passes through Point A hits the shocks at Point B. By losing angular momentum there, it starts to move radially in and crosses the ILR at Point C. The radial velocity of the inflowing gas at Point C is rather large at $\sim 63 \text{ km s}^{-1}$. The associated ram pressure is larger, by about a factor of 40 and 4, respectively, than the thermal pressure and the bar torque at the ILR that may try to stop the inflowing motion of the gas. Thus, the inflowing gas is not halted at the ILR and continues to move inward. At the same time, the gas rotates gradually faster at the expense of the gravitational potential energy. It is at Point D that the gas achieves its rotational velocity comparable to the equilibrium value and subsequently makes a closed-loop orbit, finally forming a nuclear ring. The mean radius of the ring in Model M08R20N is $r_{\text{ring}} \sim 1.4 \text{ kpc}$, well inside the ILR. Models with a more massive bar forms a ring closer to the center, owing to a larger loss of angular momentum. All rings form at the position where the centrifugal force balances the external gravity. These imply that the formation of nuclear rings is not determined by the ILR, but by the centrifugal barrier that the gas driven inward by the bar torque cannot overcome.

The upper panels of Figure 10 show the temporal and radial variation of the azimuthally-averaged surface density for all non-self-gravitating models with $\mathcal{R} = 2$, with the horizontal line indicating the ILR in each model. Various open symbols in Figure 11 plot the velocities u_y , seen in the rotating frame with the bar, of the ring gas at $y = 0$ when the ring is beginning to form in the $\mathcal{R} = 2$ models without self-gravity. Also plotted are the y -velocities of x_1 -orbits (\dot{y}_{x_1} ; upper curves) and x_2 -orbits (\dot{y}_{x_2} ; lower curves) when they cut the x -axis. For fixed \mathcal{R} , a model with larger f_{bar} has a shallower external potential Φ_{ext} and thus a lower value of \dot{y}_{x_1} and \dot{y}_{x_2} at the same x . A small solid circle at the tip of each of the lowest two curves marks the outermost x_2 -orbit beyond which no x_2 -orbit exists in that model.

As mentioned before, the ring in Model M08R20N with $f_{\text{bar}} = 0.08$ begins to form at $t \sim 0.25 \text{ Gyr}$. Already at this time, the ring material has a velocity very similar to that of an x_2 -orbit at the ring position (open circles in Fig. 11). Since the bar torque is quite weak, the angular momentum of the gas that is subsequently added to the ring is not much different from that of the gas already in the ring, keeping r_{ring} almost unchanged with time (Fig. 10a). As f_{bar} (or Q_b) increases, rings form earlier and locate closer to the center. For instance, the ring in Model M30R20N with $f_{\text{bar}} = 0.3$ begins to form at $r_{\text{ring}} \sim 1.2 \text{ kpc}$ when $t \sim 0.15 \text{ Gyr}$, with $u_y \simeq \dot{y}_{x_2} \ll \dot{y}_{x_1}$ (open squares in Fig. 11). With a considerable loss of angular momentum at the dust-lane shocks, the gas newly added to the ring has increasingly lower angular momentum, causing it to shrink with time. In addition, thermal pressure perturbations make the orbits of ring material deviate from x_2 -orbits. Some gases at the inner parts of the ring even take on x_1 -orbits. This causes the ring not only to be distributed more widely but also to shrink with time as it loses further angular momentum due to supersonic collisions of the gases on x_1 - and x_2 -orbits. Yet, the decreasing rate of the ring radius is still quite small at $d \ln r_{\text{ring}} / dt \sim -0.1 \text{ Gyr}^{-1}$ in Model M15R20N

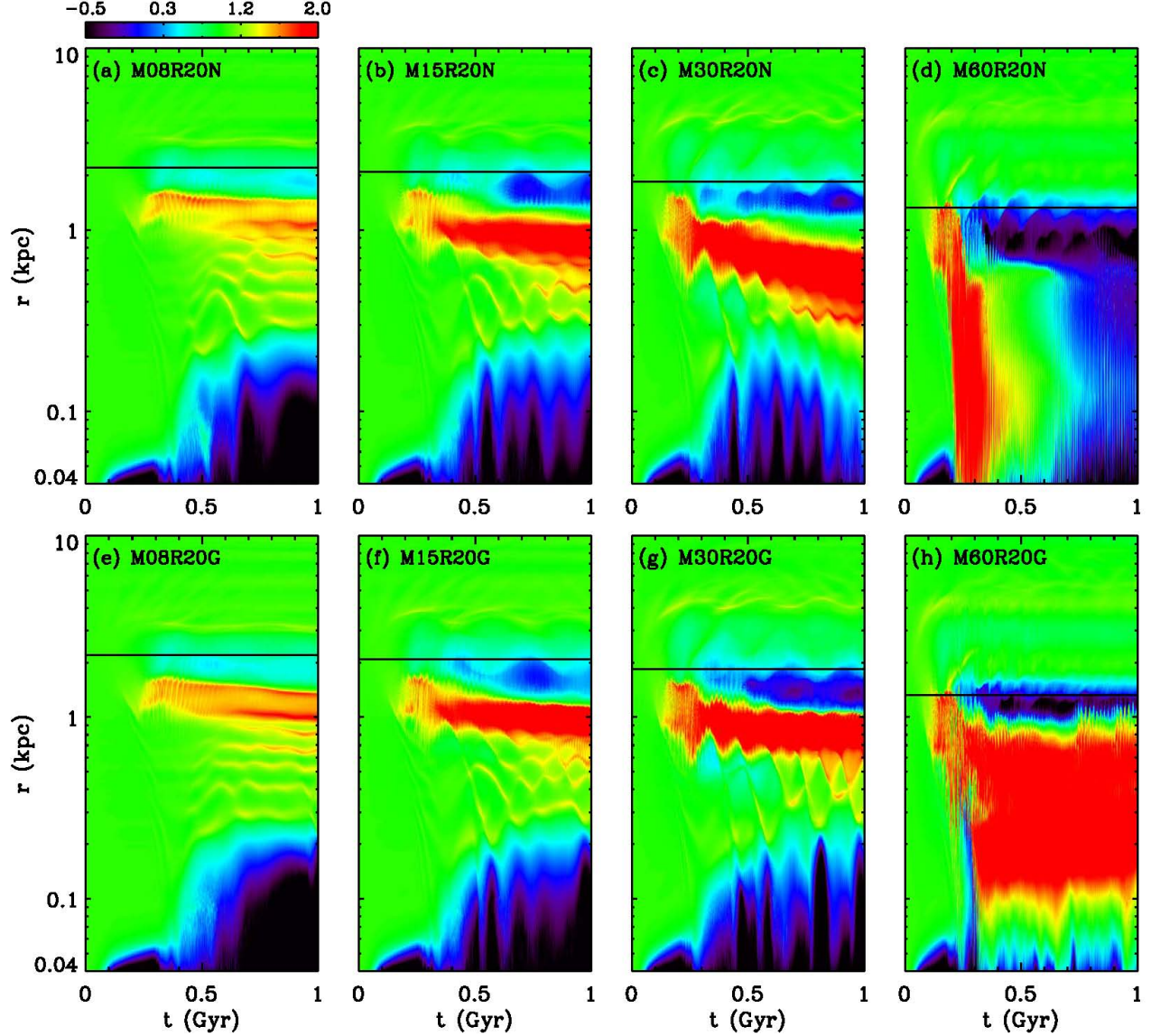


Figure 10. Temporal changes of the azimuthally-averaged surface density, $\langle \Sigma \rangle$, in logarithmic scale for all models with $\mathcal{R} = 2.0$. The upper row is for the non-self-gravitating models, while the lower row is for the self-gravitating counterparts. The horizontal line in each panel represents the location of the ILR. Color bar labels $\log(\langle \Sigma \rangle / \Sigma_0)$.

and $\sim -0.4 \text{ Gyr}^{-1}$ in Model M30R20N. In these models, rings are still of the x_2 type (Fig. 8b).

In Model M60R20N with $f_{\text{bar}} = 0.6$, on the other hand, a large bar torque takes the inflowing gas to $r_{\text{ring}} \sim 0.9 \text{ kpc}$ with velocity $u_y \sim 190 \text{ km s}^{-1}$, which is just in between $\dot{y}_{x_1} = 272 \text{ km s}^{-1}$ and $\dot{y}_{x_2} = 109 \text{ km s}^{-1}$ at that location (open triangles in Fig. 11). Since $u_y \gg \dot{y}_{x_2}$, the inflowing gas is unable to settle on an x_2 -orbit: the ring gas instead follows a hybrid orbit that is inclined by about $\phi_{\text{ring}} \sim 17^\circ$ with respect to the x -axis at $t \sim 0.12 \text{ Gyr}$. With a subsequent addition of low angular-momentum gas from outside, the ring shrinks and becomes more eccentric and inclined with time. The ring position angle is increased to $\phi_{\text{ring}} \sim 40^\circ$ at $t \sim 0.2 \text{ Gyr}$ when the ring becomes very eccentric to touch the inner boundary and starts to lose a significant amount of its mass through the inner boundary (Fig. 10d). At the same time, the inclined ring precesses slowly in the clockwise direction due to the bar torque that tends to align

the ring parallel to its major axis (see Kim & Stone 2012 for the precession of a ring in magnetized models). Figure 8c shows that the position angle of the ring in Model M60R20N is $\phi_{\text{ring}} \sim 65^\circ$ at $t = 0.3 \text{ Gyr}$, which eventually becomes 90° at $t \sim 0.38 \text{ Gyr}$ (i.e., x_1 -type ring).

The dominance (or absence) of the x_1 family of the gaseous orbits in our non-self-gravitating simulations appears to be determined not only by the amount of angular momentum loss at dust-lane shocks but also by the kinetic energies of x_1 - and x_2 -orbits allowed under a given external potential. The former is measured by Q_b , while the latter is affected by \mathcal{R} . For example, Figure 2s shows that Model M30R35N with $Q_b = 0.39$ still possesses a well-defined x_2 -type ring. In this model, Q_b is large enough to decrease the velocity of the ring material, while \mathcal{R} (together with f_{bar}) sets x_1 - and x_2 -orbits such that the rotational velocity of the ring material is larger than \dot{y}_{x_2} only slightly, but much less than \dot{y}_{x_1} , leading to an x_2 -type ring. With an even larger

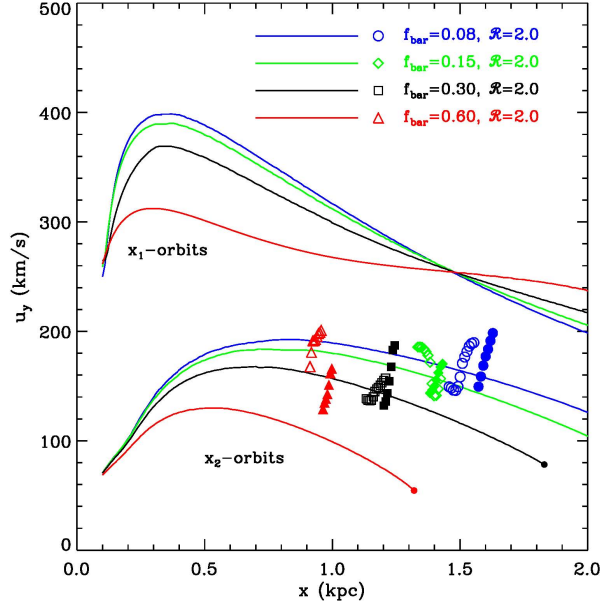


Figure 11. Distributions of y -velocities in the rotating frame of x_1 -orbits (upper curves) and x_2 -orbits (lower curves) at $y = 0$ as functions of x . Various symbols plot the numerical data of the nuclear ring at $y = 0$ when it begins to form at $t = 0.25$ Gyr for Model M08R20 (circles), $t = 0.20$ Gyr for Model M15R20 (triangles), $t = 0.15$ Gyr for Model M30R20, and $t = 0.12$ Gyr for Model M60R20. Open and filled symbols give the results for the non-self-gravitating and self-gravitating models, respectively. A small dot at the tip of each of the lowest two curves denotes the outermost x_2 -orbit in that model.

value of $Q_b = 0.67$, the ring in Model M60R35N has $u_y \sim 120 \text{ km s}^{-1}$ at $r \sim 0.8 \text{ kpc}$ when it begins to shape at $t = 0.08 \text{ Gyr}$. However, this model has the outermost x_2 -orbit at $x_c = 0.43 \text{ kpc}$, so that the ring material has no choice but to follow x_1 -orbits. The ring subsequently becomes smaller and more eccentric as low angular-momentum gas is continuously added. As the ring material directly plunges through the inner boundary, it rapidly decays at a rate $d \ln r_{\text{ring}}/dt \sim -15 \text{ Gyr}^{-1}$. In this model, most of the ring gas is accreted to the center by $t \sim 0.25 \text{ Gyr}$, with a small quantity of gas in filamentary shapes moving about the center along x_1 -rather than x_2 -orbits.

4.3.2. Effects of Self-gravity

Nuclear rings form typically at $r \sim 0.5 - 1.5 \text{ kpc}$. Equation (3) suggests that a ring could possibly be gravitationally unstable if its peak density exceeds $\sim 500 \text{ M}_\odot \text{ pc}^{-2}$.³ This happens in most of our self-gravitating models except for Models M08R15G and M15R15G where the bar torque with $Q_b \lesssim 0.04$ is too weak to cause significant gas inflows to the central regions. If a ring were uniform in models with $Q_b \gtrsim 0.05$, it would have been prone to gravitational fragmenta-

³ If the density enhancement occurs in an angular-momentum-conserving fashion, $\kappa \propto \Sigma^{1/2}$ and $Q_T \propto \Sigma^{-1/2}$ as in the case of spiral shocks (e.g., Balbus & Cowie 1985; Kim & Ostriker 2002). Rings in barred galaxies form by gathering material that *lost* angular momentum by a non-axisymmetric bar torque as well as shocks. In our models, we found κ calculated from the azimuthally-averaged rotational velocity is similar to its initial profile, suggesting that density compression in the ring does not alter κ much.

tion. However, rings are already clumpy even in non-self-gravitating models as a result of the wobble instability of dust-lane shocks. In models with intermediate bar torque (i.e., $Q_b \sim 0.1 - 0.2$), therefore, clumps in nuclear rings simply acquire more mass and become denser due to self-gravity. In models with $Q_b \gtrsim 0.2$, self-gravity produces additional fragments that make rings more clumpy in comparisons with non-self-gravitating counterparts (see, e.g., Figs. 2k and 3k). The typical mass of clumps produced is $\sim 10^6 - 10^7 \text{ M}_\odot$. We note that the maximum density such clumps can attain is limited by numerical resolution. Self-gravitating clouds are resolved only when $\Delta r < \lambda_J/4$ (Truelove et al. 1997, 1998), where Δr is the grid spacing and $\lambda_J = c_s^2/(G\Sigma)$ is the local Jeans length. Therefore, clumps with $\Sigma \gtrsim 10^3 \text{ M}_\odot \text{ pc}^{-2}$ at $r \sim 1 \text{ kpc}$ are gravitationally unresolved in our simulations.

Another important effect of self-gravity is that it makes nuclear rings larger compared to those in non-self-gravitating models. Figures 8 and 10 show that compared to in Model M30R20N, the ring in Model M30R20G is larger in size at $t = 0.3 \text{ Gyr}$ and decays less afterward (see also Fig. 4). This is because self-gravity deepens the total gravitational potential at the location of a ring, making the orbits of the ring material relatively intact and resistant to external perturbations that tend to change the orbits. Therefore, the radial decay of a ring due to the addition of low angular-momentum gas from outside is slower in self-gravitating models. The effect of thermal pressure in dispersing the ring material spatially is also smaller, resulting in a narrower and larger ring than in non-self-gravitating models.

Finally, we discuss rings in self-gravitating models with a massive bar ($f_{\text{bar}} = 0.6$). Figure 8 shows that Model M60R20G possesses x_2 -type, double rings at $t = 0.3 \text{ Gyr}$, which is unlike Model M60R20N that has an inclined, single ring. As explained above, a large bar torque in Model M60R20N produces an inclined ring at $t \sim 0.12 \text{ Gyr}$ that processes with time to become of the x_1 -type. Strong self-gravity in Model M60R20G prevents the precession of the ring by providing additional non-axisymmetric torque, gradually aligning its long axis parallel to the bar minor axis. At $t = 0.22 \text{ Gyr}$, the ring is still quite eccentric and forms many high-density clumps via gravitational instability. When dense (unresolved) clumps move close to the galaxy center on their orbits ($t \sim 0.26 \text{ Gyr}$), they gravitationally interact with other clumps at the opposite side. These interacting clumps lower their orbits to smaller r , gather gas from the ring outside, and form an inner ring at $t = 0.29 \text{ Gyr}$. The inner ring slowly dissipates as it loses mass through the inner boundary. In Model M60R25G, self-gravity results in an x_2 -type ring. But, the ring in this model is already so small that the gravitational interaction of dense clumps do not produce an obvious inner ring. Small, x_2 -type rings in Models M60R30G and M60R35G (Fig. 3p,t) become weaker with time and vanish at $t \sim 0.75 \text{ Gyr}$, so that they are not considered as being permanent (Fig. 4p).

4.3.3. Ring Properties

To quantify the ring properties, we at each time calculate the mean density Σ_{ring} , mean radius r_{ring} , ellipticity $\epsilon_{\text{ring}} = 1 - b_r/a_r$ with a_r and b_r denoting the semi-major and minor axes, respectively, and the position angle ϕ_{ring}

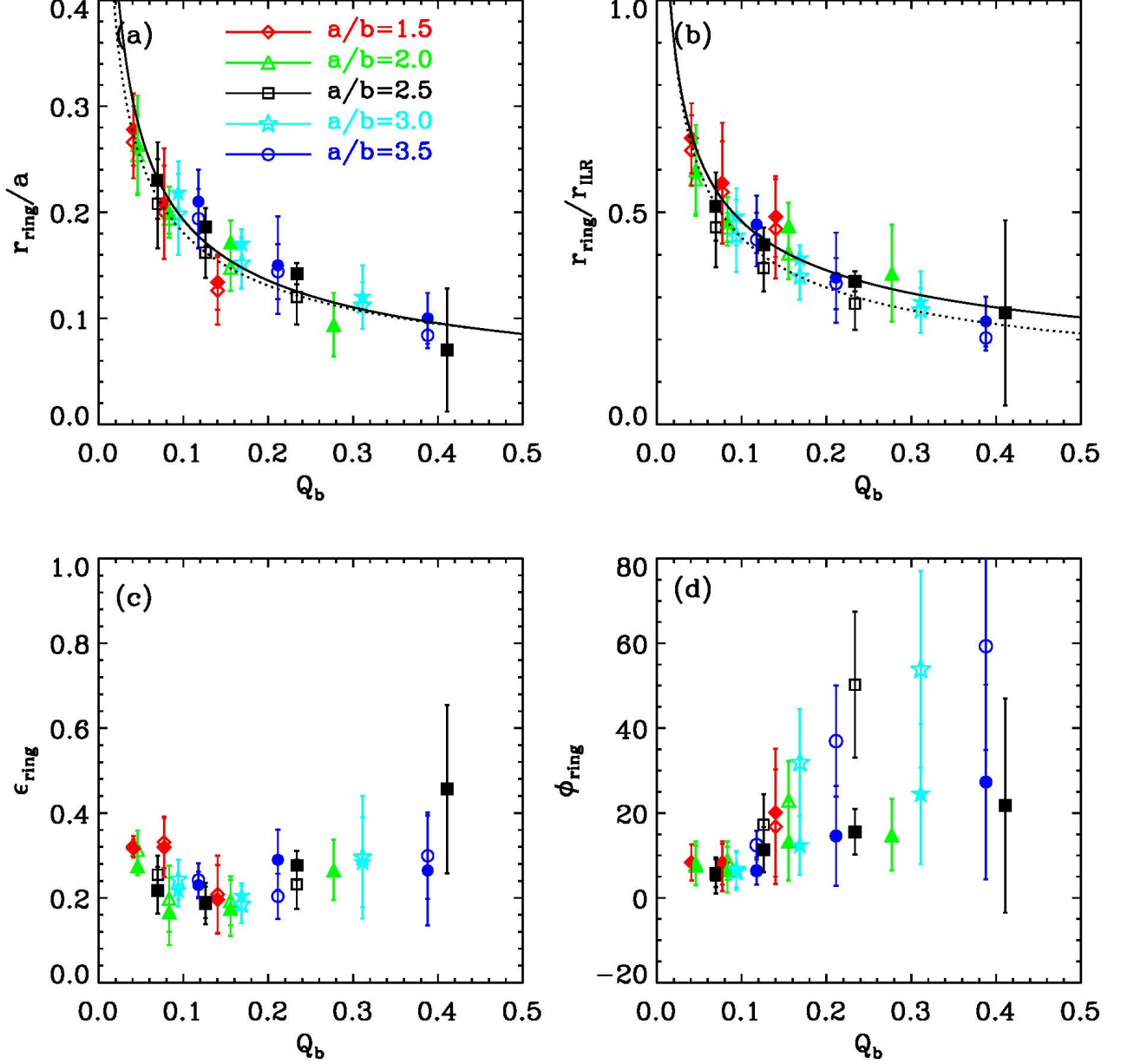


Figure 12. Dependence on the bar strength Q_b of the ring size r_{ring} relative (a) to the bar semimajor axis a and (b) to the ILR radius r_{ILR} , (c) the ring ellipticity ϵ_{ring} , and (d) the ring position angle ϕ_{ring} for models with x_2 -type rings. In each panel, symbols give the mean values averaged over $t = 0.3$ – 1.0 Gyr, while errorbars represent the standard deviations. Open and filled symbols are for non-self-gravitating and self-gravitating models, respectively. Dotted and solid lines in (a) and (b) draw equations (9) and (10) for non-self-gravitating and self-gravitating models, respectively.

of the long axis of the ring, and take their temporal averages over $t = 0.3$ – 1.0 Gyr. The resulting mean values and standard deviations are given in Tables 3 and 4 for non-self-gravitating and self-gravitating models, respectively. Figure 12 plots these as various symbols and errorbars as functions of Q_b for models with x_2 -type rings. Open symbols are for the non-self-gravitating models, while the self-gravitating results are plotted as filled symbols. It turns out that r_{ring} is best fitted solely by Q_b not in combination with \mathcal{R} . Our best fits of r_{ring} against Q_b are

$$\frac{r_{\text{ring}}}{a} = \begin{cases} 0.062Q_b^{-0.46}, & \text{without self-gravity,} \\ 0.059Q_b^{-0.51}, & \text{with self-gravity,} \end{cases} \quad (9)$$

in terms of the bar major axis, and

$$\frac{r_{\text{ring}}}{r_{\text{ILR}}} = \begin{cases} 0.16Q_b^{-0.45}, & \text{without self-gravity,} \\ 0.19Q_b^{-0.40}, & \text{with self-gravity,} \end{cases} \quad (10)$$

in terms of the ILR radius.

Equations (9) and (10) are plotted in Figure 12a,b as dotted and solid lines for non-self-gravitating and self-gravitating models, respectively. Overall, rings in self-gravitating models are about ~ 5 – 20% larger than in non-self-gravitating models. The decrease of r_{ring} with Q_b is of course due to the fact that a stronger bar torque drives the gas closer to the galaxy center by removing

Table 3
Properties of Nuclear Rings in Non-self-gravitating Models

Model	$\Sigma_{\text{ring}}/\Sigma_0$	r_{ring} (kpc)	ϵ_{ring}	ϕ_{ring} (deg)
M08R15N
M08R20N	1.5 ± 0.2	1.27 ± 0.19	0.31 ± 0.05	7.6 ± 4.7
M08R25N	4.1 ± 1.5	1.04 ± 0.21	0.25 ± 0.05	5.3 ± 4.3
M08R30N	5.1 ± 1.8	0.99 ± 0.19	0.24 ± 0.05	6.2 ± 4.4
M08R35N	4.6 ± 2.0	0.97 ± 0.14	0.24 ± 0.04	12.4 ± 3.4
M15R15N	1.5 ± 0.3	1.33 ± 0.17	0.32 ± 0.02	8.3 ± 4.3
M15R20N	3.6 ± 1.4	0.97 ± 0.07	0.20 ± 0.08	8.8 ± 4.6
M15R25N	9.3 ± 4.4	0.81 ± 0.12	0.19 ± 0.05	17.2 ± 7.2
M15R30N	9.8 ± 3.9	0.76 ± 0.12	0.18 ± 0.04	31.9 ± 12.6
M15R35N	14.1 ± 9.8	0.72 ± 0.13	0.20 ± 0.05	36.9 ± 13.1
M30R15N	2.5 ± 0.8	1.00 ± 0.22	0.33 ± 0.06	7.1 ± 5.6
M30R20N	8.2 ± 4.4	0.74 ± 0.11	0.19 ± 0.06	22.9 ± 9.3
M30R25N	22.9 ± 13.0	0.60 ± 0.13	0.23 ± 0.06	50.2 ± 17.2
M30R30N	28.9 ± 14.0	0.56 ± 0.11	0.30 ± 0.14	53.8 ± 23.2
M30R35N	38.0 ± 12.4	0.42 ± 0.06	0.30 ± 0.10	59.3 ± 24.5
M60R15N	4.6 ± 2.5	0.63 ± 0.16	0.21 ± 0.09	16.8 ± 13.5
M60R20N	1.4 ± 1.2	0.15 ± 0.10	0.63 ± 0.22	36.0 ± 36.7
M60R25N	0.8 ± 2.0	0.21 ± 0.14	0.47 ± 0.17	87.8 ± 17.3
M60R30N
M60R35N

Note. — Σ_{ring} , r_{ring} , ϵ_{ring} and ϕ_{ring} denote the mean density, mean radius, ellipticity, and position angle of the long axis of a ring, respectively.

larger angular momentum from it. Note that $r_{\text{ring}}/r_{\text{ILR}}$ is less than unity and can be as small as ~ 0.2 , demonstrating again that the ring position is not determined by the ILR but by Q_b . We will show in Section 5 that the decreasing tendency of r_{ring} with Q_b is qualitatively consistent with the observational results of Comerón et al. (2009) who found that nuclear rings are smaller in more strongly barred galaxies. In our models, nuclear rings are in general elliptical with $\epsilon_{\text{ring}} \sim 0.2$ – 0.3 , insensitive to Q_b and self-gravity. They are well aligned with the bar minor axis when $Q_b < 0.1$, while becoming more inclined as Q_b increases.

4.4. Nuclear Spirals

There are two types of perturbations that can excite nuclear spirals in the central regions: the non-axisymmetric bar potential and sonic perturbations from a nuclear ring. At early time before a ring forms, the bar potential is a lone perturbing agent of $m = 2$ spiral waves. As explained in Paper I, our galaxy models with a central BH have $d(\Omega - \kappa/2)/dr > 0$ at $r_{\text{min}} \leq r \leq r_{\text{max}}$ and $d(\Omega - \kappa/2)/dr < 0$ otherwise, with the local minimum and maximum of the $\Omega - \kappa/2$ curve occurring at $r_{\text{min}} \sim 0.2$ kpc and $r_{\text{max}} \sim 0.4$ – 0.6 kpc depending on f_{bar} and \mathcal{R} . Thus, the spiral waves at $r < r_{\text{min}}$ are trailing, while they are leading at $r_{\text{min}} \leq r \leq r_{\text{max}}$ early time. Since the bar potential is nearly axisymmetric near the center, these waves would remain weak unless additional perturbations are supplied. In models with an x_2 -type ring, a ring that forms outside the spirals provides sonic perturbations that propagate inward in the form of trailing waves. These waves interact constructively (destructively) with the trailing (leading) part of the spirals. Consequently, the outer leading parts are destroyed, while the inner trailing spirals grow stronger and extend outward to make contact with the ring (Fig. 8a,b). On the other hand, models with an x_1 -type ring do not retain nuclear spirals since the ring gas on eccentric orbits wipes out inner coherent spiral structures (Fig.

Table 4
Properties of Nuclear Rings in Self-gravitating Models

Model	$\Sigma_{\text{ring}}/\Sigma_0$	r_{ring} (kpc)	ϵ_{ring}	ϕ_{ring} (deg)
M08R15G
M08R20G	2.4 ± 1.0	1.32 ± 0.23	0.28 ± 0.02	8.2 ± 5.1
M08R25G	4.2 ± 1.5	1.15 ± 0.18	0.22 ± 0.05	5.8 ± 3.3
M08R30G	5.6 ± 1.9	1.09 ± 0.15	0.22 ± 0.04	6.7 ± 4.3
M08R35G	6.1 ± 2.2	1.05 ± 0.15	0.25 ± 0.03	6.4 ± 3.2
M15R15G	1.6 ± 0.4	1.39 ± 0.17	0.32 ± 0.02	8.3 ± 4.2
M15R20G	5.6 ± 2.3	1.00 ± 0.12	0.17 ± 0.08	6.6 ± 5.4
M15R25G	9.2 ± 4.6	0.93 ± 0.09	0.19 ± 0.04	11.3 ± 5.3
M15R30G	12.6 ± 6.0	0.85 ± 0.07	0.20 ± 0.03	12.3 ± 6.8
M15R35G	111.5 ± 56.7	0.75 ± 0.23	0.29 ± 0.07	14.6 ± 11.8
M30R15G	2.8 ± 1.1	1.04 ± 0.26	0.32 ± 0.07	8.2 ± 5.1
M30R20G	11.2 ± 5.0	0.86 ± 0.10	0.18 ± 0.07	13.4 ± 9.3
M30R25G	18.4 ± 7.5	0.71 ± 0.05	0.28 ± 0.03	15.6 ± 5.4
M30R30G	81.2 ± 23.4	0.60 ± 0.15	0.28 ± 0.11	24.4 ± 16.5
M30R35G	78.7 ± 17.1	0.50 ± 0.12	0.26 ± 0.13	27.3 ± 23.0
M60R15G	5.2 ± 2.5	0.67 ± 0.13	0.20 ± 0.08	20.1 ± 15.1
M60R20G	32.8 ± 10.0	0.47 ± 0.15	0.27 ± 0.07	14.8 ± 8.4
M60R25G	69.5 ± 10.5	0.35 ± 0.29	0.46 ± 0.20	21.8 ± 25.3
M60R30G
M60R35G

Note. — Σ_{ring} , r_{ring} , ϵ_{ring} and ϕ_{ring} denote the mean density, mean radius, ellipticity, and position angle of the long axis of a ring, respectively.

8c). Even though Model M30R35N has an x_2 -type ring, it is so small that strong perturbations from it inhibit the growth of spirals inside. Therefore, the presence of nuclear spirals requires two conditions: they should be of the x_2 type and sufficiently large (perhaps larger than r_{max}).

Unlike dust lanes and nuclear rings, both of which remain relatively stationary after the bar potential is fully turned on, we find that nuclear spirals do not achieve a quasi-steady state in that their peak density Σ_{peak} and pitch angle i_p vary substantially with time. Figure 13a,b plots the temporal changes of Σ_{peak} and i_p measured at $r = 0.2$ kpc for a few selected models. Dotted and solid lines correspond to non-self-gravitating and self-gravitating models, respectively. Compared to the other non-self-gravitating models, Model M30R25N forms nuclear spirals earlier due to a larger bar torque. In general, nuclear spirals tend to unwind (i.e., i_p increases) as they become stronger. This appears to be a generic consequence of the nonlinear effect. Lee & Goodman (1999) showed analytically that dispersion relations of nonlinear waves involve the wavenumber, frequency, and wave amplitude all together, which is unlike in the linear-wave case where the wavenumber and frequency are independent of the amplitude. They further showed that the wavenumber of nonlinear spiral waves is a decreasing function of the amplitude and that nonlinear trailing waves unwind and become more nonlinear as they propagate inward due to the increase in the angular momentum flux carried by the waves. This nonlinear growth and unwinding of traveling waves is consistent with the behavior of nuclear spirals formed in our models.

Figure 13 also shows that nuclear spirals in self-gravitating models unwind more slowly than the non-self-gravitating counterparts. This is presumably because non-axisymmetric waves corotating with the bar in self-gravitating models should have a larger radial wavenumber k_r than those in non-self-gravitating models in order to have the same frequency. With larger k_r , the an-

Table 5
Time-averaged Mass Inflow Rate and Its Dispersion

Model	\dot{M} ($M_{\odot} \text{ yr}^{-1}$)	$\Delta \dot{M}$ ($M_{\odot} \text{ yr}^{-1}$)	Model	\dot{M} ($M_{\odot} \text{ yr}^{-1}$)	$\Delta \dot{M}$ ($M_{\odot} \text{ yr}^{-1}$)
M08R15N	2.4×10^{-3}	1.7×10^{-3}	M08R15G	2.2×10^{-3}	1.6×10^{-3}
M08R20N	2.3×10^{-3}	2.1×10^{-3}	M08R20G	2.1×10^{-3}	1.9×10^{-3}
M08R25N	2.9×10^{-3}	1.9×10^{-3}	M08R25G	2.5×10^{-3}	1.7×10^{-3}
M08R30N	3.1×10^{-3}	2.1×10^{-3}	M08R30G	2.4×10^{-3}	1.5×10^{-3}
M08R35N	3.2×10^{-3}	2.0×10^{-3}	M08R35G	2.4×10^{-3}	1.3×10^{-3}
M15R15N	2.3×10^{-3}	2.1×10^{-3}	M15R15G	2.2×10^{-3}	2.0×10^{-3}
M15R20N	3.2×10^{-3}	2.2×10^{-3}	M15R20G	2.4×10^{-3}	1.8×10^{-3}
M15R25N	3.3×10^{-3}	2.3×10^{-3}	M15R25G	3.0×10^{-3}	1.9×10^{-3}
M15R30N	2.6×10^{-3}	1.7×10^{-3}	M15R30G	2.6×10^{-3}	2.3×10^{-3}
M15R35N	2.5×10^{-3}	2.3×10^{-3}	M15R35G	1.2×10^{-1}	7.7×10^0
M30R15N	3.1×10^{-3}	2.7×10^{-3}	M30R15G	2.7×10^{-3}	2.2×10^{-3}
M30R20N	5.2×10^{-3}	3.9×10^{-3}	M30R20G	2.9×10^{-3}	2.3×10^{-3}
M30R25N	2.0×10^{-3}	3.2×10^{-3}	M30R25G	4.2×10^{-3}	2.9×10^{-3}
M30R30N	2.5×10^{-2}	5.4×10^{-2}	M30R30G	3.6×10^{-1}	2.0×10^1
M30R35N	1.7×10^{-1}	2.3×10^{-1}	M30R35G	3.8×10^{-1}	1.9×10^1
M60R15N	7.5×10^{-3}	8.6×10^{-3}	M60R15G	3.9×10^{-3}	4.6×10^{-3}
M60R20N	3.2×10^{-1}	8.1×10^{-1}	M60R20G	1.2×10^{-2}	2.6×10^{-1}
M60R25N	5.4×10^{-1}	2.3×10^0	M60R25G	6.3×10^{-1}	4.3×10^1
M60R30N	8.8×10^{-1}	2.2×10^0	M60R30G	7.0×10^{-1}	3.2×10^1
M60R35N	9.2×10^{-1}	2.0×10^0	M60R35G	1.2×10^0	5.5×10^1

Note. — Time average of \dot{M} is taken over $t = 0.1 - 1.0$ Gyr.

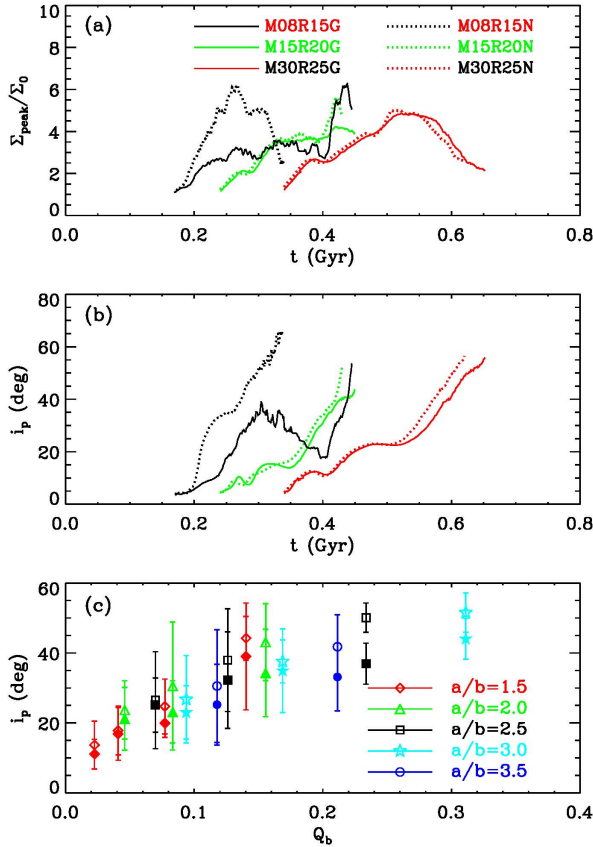


Figure 13. Temporal evolution of (a) the peak surface density Σ_{peak} and (b) the pitch angle i_p of nuclear spirals at $r = 0.2$ kpc in Models M08R15, M15R20, and M30R25. Dotted and solid lines are for non-self-gravitating and self-gravitating models, respectively. (c) Mean values (symbols) of i_p averaged over $t = 0.3 - 0.5$ Gyr with the standard deviations (errorbars) as a function of Q_b for all models with nuclear spirals. Open and filled symbols are for non-self-gravitating and self-gravitating models, respectively.

gle between the gas streamlines and nuclear spirals are smaller in self-gravitating models. This leads to a smaller departure of gas trajectories from the circular motions, resulting in lower Σ_{peak} .

All nuclear spirals in our models are logarithmic in shape. They grow with time and eventually develop into shocks, with the shock formation epoch delayed progressively with decreasing Q_b . For instance, the spirals in Models M30R25N, M15R20N, and M08R15N become shocks at $t \sim 0.26, 0.42$, and 0.50 Gyr, respectively, after which Σ_{peak} decreases as most of the central gas inside the ring is accreted through the inner boundary. The shock formation time of nuclear spirals are delayed to $t \sim 0.43, 0.45$, and 0.55 Gyr for self-gravitating Models M30R25G, M15R20G, and M08R15G, respectively. At a given time, therefore, the nuclear spirals in smaller- Q_b models tend to be more tightly wound, while those in larger- Q_b models tend to be more open and, sometimes, even shocked (Fig. 8). This is illustrated quantitatively in Figure 13c where the temporal averages of i_p and the standard deviations over $t = 0.3 - 0.5$ Gyr are plotted for models with appreciable spirals during this time interval. The increasing behavior of i_p with Q_b is consistent with the observational result of Peebles & Martini (2006) that nuclear spirals tend to be tightly wound in weakly barred galaxies.

4.5. Mass Inflow Rate

A galactic bar has often been considered to be a powerful means to transport the interstellar gas at $\sim \text{kpc}$ scales all the way to the galaxy center, fueling AGN. To check the viability of this idea using our models, Figures 14 and 15, for non-self-gravitating and self-gravitating models, respectively, plot the mass inflow rates \dot{M} through the inner boundary as functions of time. Table 5 gives the time-averaged values of \dot{M} and the standard deviations $\Delta \dot{M}$ over $t = 0.1 - 1.0$ Gyr for all models. One should be

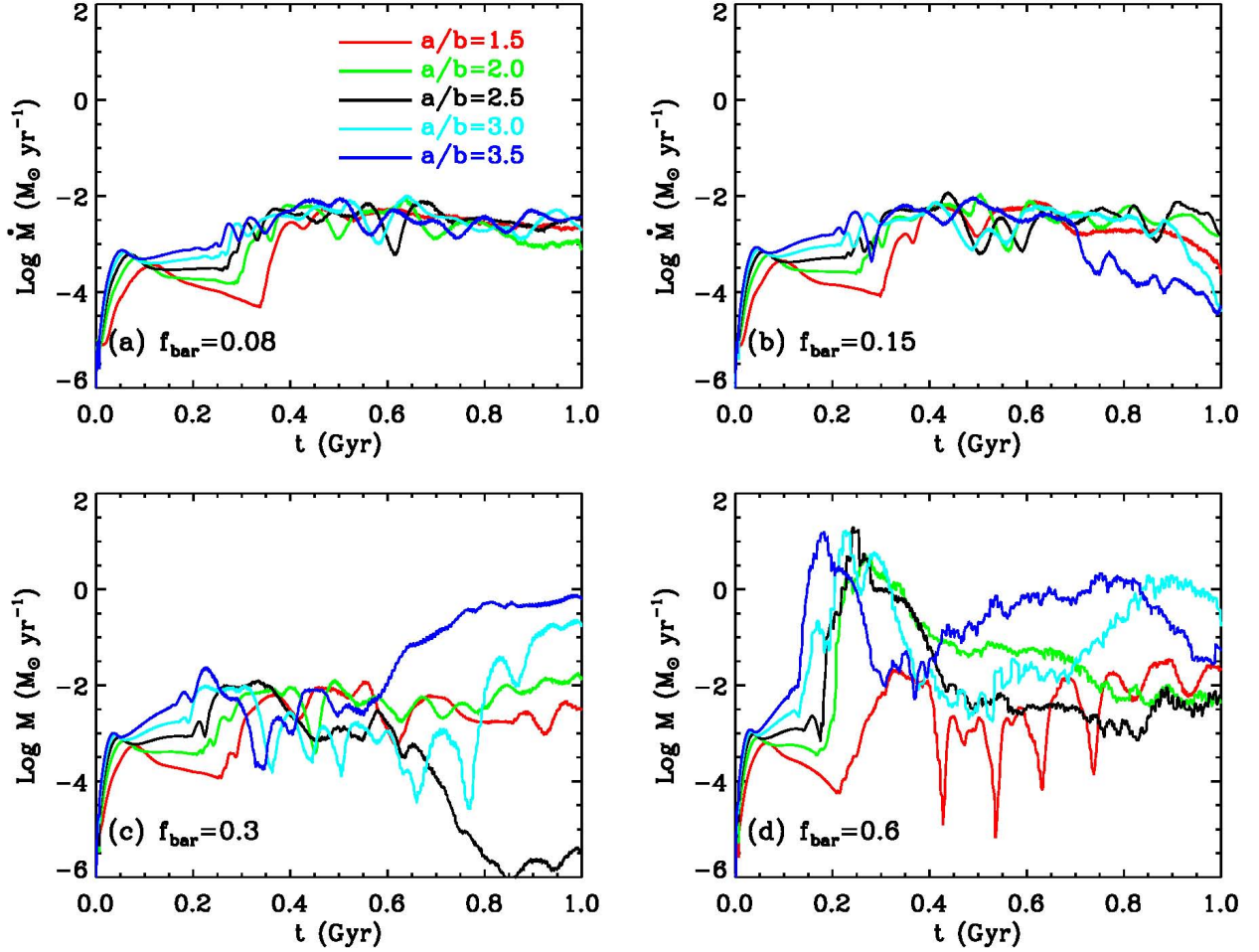


Figure 14. Temporal variations of the mass inflow rates \dot{M} for non-self-gravitating models with (a) $f_{\text{bar}} = 0.08$, (b) $f_{\text{bar}} = 0.15$, (c) $f_{\text{bar}} = 0.3$, and (d) $f_{\text{bar}} = 0.6$.

cautious in relating \dot{M} to the accretion rate to a central BH, since the inflowing gas through the inner boundary may change its orbit due possibly to thermal and radiation pressures, gravity, etc. before reaching a BH and then come out of the inner boundary, or may be lost to star formation in a circumnuclear disk surrounding a BH (e.g., Kawakatu & Wada 2008), which are not captured in our simulations. Therefore, \dot{M} calculated from the current models can be considered as upper limits to the real accretion rates to a central BH.

In non-self-gravitating models with a well-defined x_2 -type ring, \dot{M} is quite small at $\sim 10^{-4} - 10^{-3} M_{\odot} \text{ yr}^{-1}$ at early time before the dust-lane shocks fully develop. It then increases as the gas flows inward along the dust lanes, but only to $\sim 10^{-3} - 10^{-2} M_{\odot} \text{ yr}^{-1}$ unless the bar is strongly elongated with $\mathcal{R} \gtrsim 3.0$. These relatively small values of \dot{M} result from the fact that the majority of the inflowing gas from dust lanes is trapped in a nuclear ring that is located away from the center. Late time evolution of \dot{M} depends on the size of a ring. In models with $r_{\text{ring}} \gtrsim 0.5$ kpc, \dot{M} remains below $\sim 10^{-2} M_{\odot} \text{ yr}^{-1}$. In Model M30R25N, on the other hand, the ring decays with time to have $r_{\text{ring}} \sim 0.4$ kpc at $t = 0.6$ Gyr. At this small radius, thermal pressure is efficient to perturb x_2 -like gas orbits into eccentric shapes, increasing \dot{M} to

$\sim 1 M_{\odot} \text{ yr}^{-1}$ at $t \gtrsim 0.8$ Gyr.

For models whose central regions are dominated by x_1 -orbits, on the other hand, \dot{M} increases dramatically to above $\sim 1 M_{\odot} \text{ yr}^{-1}$, and sometimes as large as $\sim 10 M_{\odot} \text{ yr}^{-1}$, as an inclined ring becomes smaller and more eccentric. When the short axis of an eccentric ring touches the inner boundary, the ring material flows in directly through it. This in turn causes the ring to decay rapidly in time, making \dot{M} drop to $\sim 10^{-2} - 10^{-1} M_{\odot} \text{ yr}^{-1}$. In Model M60R30N, gaseous blobs located in between the ring and the bar ends gradually move in toward the center and orbit along x_1 -orbits in the vicinity of the hole, which increases \dot{M} again to $\sim 1 M_{\odot} \text{ yr}^{-1}$ at $t = 0.8$ Gyr.

In self-gravitating models with $Q_b \lesssim 0.2$, \dot{M} is slightly smaller, owing to a larger nuclear ring, than that in the non-self-gravitating counterpart. In models with $Q_b \gtrsim 0.2$, however, self-gravity makes the rings unstable, producing small dense clumps. While these clumps move along the rings, they interact with each other and sometimes plunge into the central hole directly, increasing \dot{M} instantaneously. In Model M15R35G with $Q_b = 0.21$, such events occurring three times over 1 Gyr lead to $\dot{M} > 10^2 M_{\odot} \text{ yr}^{-1}$. In other models with larger Q_b such as Models M30R30G and M60R35G, direct accretion of dense clumps occur much more frequently, making the

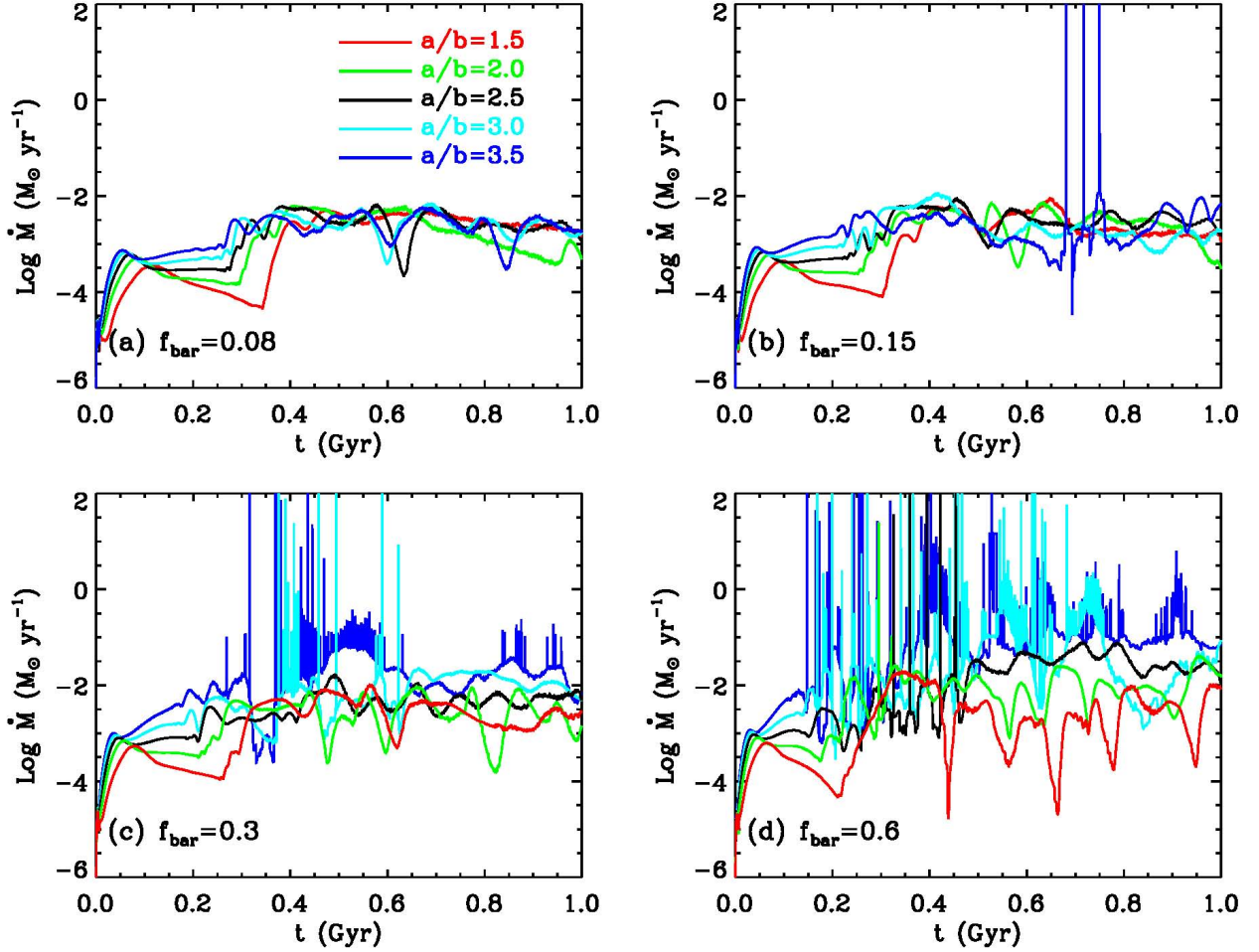


Figure 15. Same as Figure 14, but for self-gravitating models. \dot{M} curves *vs.* time highly intermittent.

5. SUMMARY AND DISCUSSION

We have presented the results of high-resolution hydrodynamic simulations on the formation and evolution of gaseous substructures in barred galaxies with varying bar strength. We initially consider an infinitesimally-thin, isothermal, unmagnetized gas disk with uniform surface density embedded in the external gravitational potential. We run both non-self-gravitating and self-gravitating models, but the effects of star formation and feedback are not considered in the present work. In order to focus on the effects of the bar parameters, we fix the gas sound speed to $c_s = 10 \text{ km s}^{-1}$ and the BH mass to $M_{\text{BH}} = 4 \times 10^7 M_\odot$ that affects the rotation curve near the galaxy center, and vary two parameters: the bar mass measured by f_{bar} (Eq. [2]) relative to the spheroidal component and its aspect ratio \mathcal{R} (see Tables 1 and 2 for model parameters).

In what follows, we summarize the main results of the present work and discuss them in comparison with observations.

1. Bar Strength Parameter – We measure the bar strength using the dimensionless parameter Q_b (Eq. [4]) as is usually done in observational studies. For our galaxy models with a Ferrers prolate bar with index n , we calculate Q_b as well as the radius $r(Q_b)$ where the maximum bar torque occurs, and provide the fitting formulae (Eqs.

[5] and [6]) as functions of f_{bar} and \mathcal{R} . While Q_b is linearly proportional to \mathcal{R} and almost linearly to f_{bar} , $r(Q_b)$ is a weakly decreasing function of \mathcal{R} and independent of f_{bar} . Both Q_b and $r(Q_b)$ become smaller for a more centrally-concentrated bar.

Having found the dependence of Q_b and $r(Q_b)$ on the other bar parameters in our galaxy models, it is interesting to apply our results to observed barred galaxies. Recently, Comerón et al. (2010) measured Q_b , $r(Q_b)$, \mathcal{R} (or, equivalently, the bar ellipticity), and the bar semi-major axis a for a sample of nearby galaxies that contain nuclear rings, which is by far the most complete sample. Figure 16a plots as star symbols the empirical relation between Q_b and \mathcal{R} from Comerón et al. (2010) for galaxies with $1.5 \leq \mathcal{R} \leq 3.5$. Also plotted are equation (5) for various values of n and f_{bar} . Note that the trend of Q_b becoming larger for larger \mathcal{R} in the observational estimates is entirely consistent with the results of our galaxy models.

When approximating the observed bars using Ferrers prolate spheroids, the observational results for Q_b *vs.* \mathcal{R} can be best described by the bar mass fraction of $f_{\text{bar}} = 0.3\text{--}0.5$ for $n = 1$ inhomogeneous bars and $f_{\text{bar}} = 0.25\text{--}0.35$ for $n = 0$ homogeneous bars. The observed relation between $r(Q_b)/a$ and \mathcal{R} shown in Figure 16b appears better explained by the $n = 0$ homo-

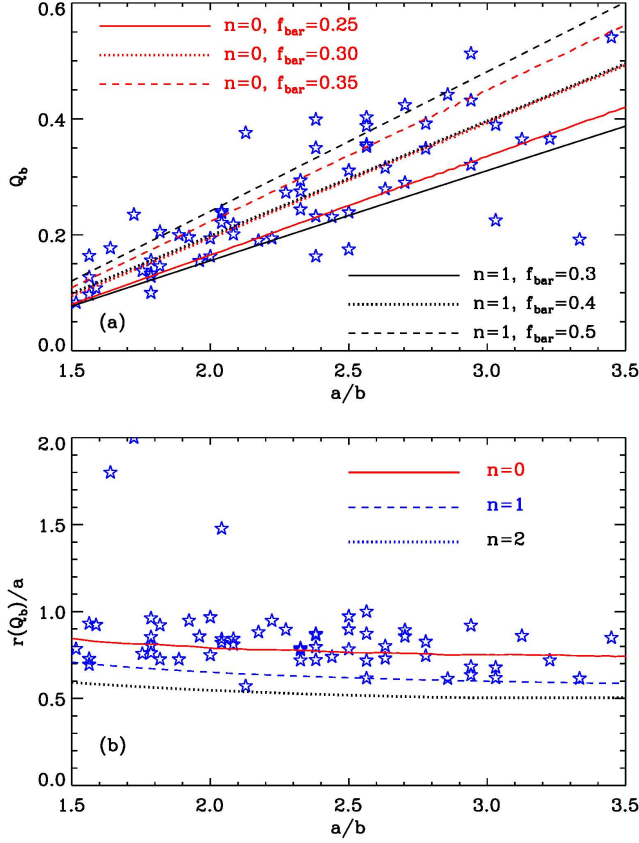


Figure 16. Relationships (a) between Q_b and $\mathcal{R} = a/b$ and (b) between $r(Q_b)$ and \mathcal{R} from our galaxy models (various lines) with a Ferrers prolate bar (Eqs. [5] and [6]) in comparison with observational results (star symbols) of Comerón et al. (2010). The observed bars are best represented by $f_{\text{bar}} = 0.25\text{--}0.5$ and $n \leq 1$.

geneous bars than inhomogeneous bars.⁴ We note that many uncertainties surround the observational determinations of Q_b and $r(Q_b)$ as they rely sensitively on the bulge subtraction, assumptions on the disk scale height and orientation angle, etc., which are quite uncertain (e.g., Laurikainen et al. 2004, 2006; Buta et al. 2006). Given that observational errors involved in the Q_b (also likely in $r(Q_b)$) determinations are typically $\sim 20\%$ (e.g., Comerón et al. 2009), the comparison shown in Figure 16 suggests that bars in real galaxies are most likely to have a mass fraction $f_{\text{bar}} = 0.25\text{--}0.5$ of the spheroidal component, and unlikely to be more centrally concentrated than the $n = 1$ case.

2. *Dust Lanes* – The imposed non-axisymmetric bar potential readily induces dust-lane shocks across which gas in rotation about the galaxy center loses angular momentum significantly and falls radially inward. Dust lanes in a quasi-steady state approximately follow one of x_1 -orbits aligned parallel to the bar major axis. The curvature $\Delta\alpha$ of dust lanes in our models depends primarily on Q_b in such a way that they tend to be more curved under a weaker bar. This results from the facts that dust lanes are closer to the bar major axis as Q_b increases and that inner x_1 -orbits are more eccentric than outer ones

⁴ Galaxies with $r(Q_b)/a > 1$ have non-axisymmetric torques dominated by outer spiral arms rather than by bars (Comerón et al. 2010).

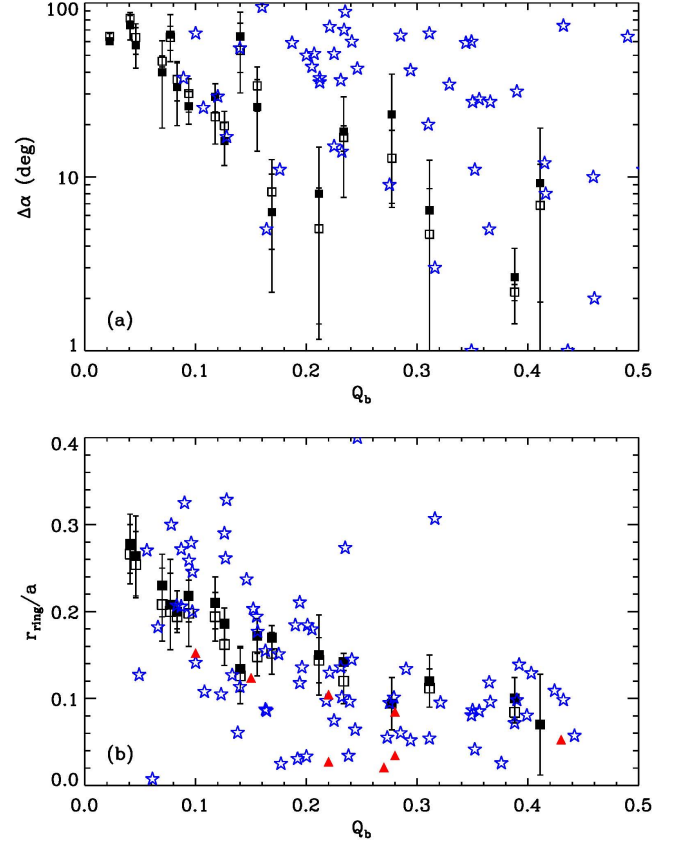


Figure 17. Comparison of our numerical results (squares with errorbars) with the observational measurements for the relations (a) between the dust-lane curvature $\Delta\alpha$ and Q_b and (b) between the ring radius r_{ring} and Q_b . Open and filled squares are for non-self-gravitating and self-gravitating models, respectively. In (a), star symbols are adopted from Comerón et al. (2009), while star symbols and filled triangles in (b) are from Comerón et al. (2010) and Mazzuca et al. (2011), respectively.

(see Fig. 7). It also depends, albeit less sensitively, on \mathcal{R} in that a more elongated bar has more straight dust lanes (Eq. [8]), since x_1 -orbits are rounder with smaller \mathcal{R} when Q_b is fixed. Dust lanes are not much affected by self-gravity since they have a Toomre stability parameter greater than unity and are characterized by strong velocity shear.

As mentioned earlier, that dust lanes are more straight under a stronger bar potential was first theoretically predicted by Athanassoula (1992b) and later confirmed empirically by Knapen et al. (2002) and Comerón et al. (2009). In particular, Comerón et al. (2009) measured the dust-lane curvatures in a sample of 55 barred galaxies that contain clear dust lanes in the SDSS DR7 or NED images, and studied a relationship between $\Delta\alpha$ and Q_b . Figure 17a reproduces their observational results as star symbols in comparison with our numerical results shown as open and filled squares with errorbars for non-self-gravitating and self-gravitating models, respectively. Note that $\Delta\alpha$ decreases with increasing Q_b in both numerical and observational results, although $\Delta\alpha$ in the simulations corresponds roughly to the lower envelope of the observational results. Note also that our numerical results are unable to reproduce the scatter seen in the observations. These quantitative differences of $\Delta\alpha$ be-

tween our numerical work and the work of Comerón et al. (2009) are likely due to the differences in the spatial ranges of dust lanes where $\Delta\alpha$ is measured. Comerón et al. (2009) considered a constant-curvature range that varies from galaxy to galaxy, while we fix the position angles of both ends of the range. Also, the fact that the parameter space covered by our models is very limited (i.e., fixed sound speed, $n = 1$ Ferrers bar potential, no magnetic field, etc.) may also be partly responsible for the differences between our numerical results and the observations.

Comerón et al. (2009) further noted that there is a large spread of $\Delta\alpha$ for given Q_b . To find the origin of the spread, they ran a large number of numerical simulations with differing bar and bulge parameters, and found that the spread in $\Delta\alpha$ can be reduced if the aspect ratio \mathcal{R} is considered together with Q_b when fitting the curvatures. We similarly found that a linear combination of Q_b and \mathcal{R} provides a better fit than Q_b alone, although $\Delta\alpha$ decreases with increasing \mathcal{R} in our fit (Eq. [8]), while $\Delta\alpha$ is an increasing function of \mathcal{R} in their fit (Eq. [3] of Comerón et al. 2009). This discrepancy is again thought of as arising from the differences in the ranges of dust lanes where $\Delta\alpha$ is measured and from the limited range of the parameter space in our models, as mentioned above.

3. Nuclear Rings: Size – The shocked gas moving in toward the central regions along the dust lanes has so large a speed that the bar torque cannot stop its motion across the ILR. The inflowing gas keeps moving in and eventually forms a nuclear ring at the location where the centrifugal force balances the external gravitational force. The mean radius of a ring in our models is generally smaller than the ILR location, and decreases systematically with increasing Q_b (Eqs. [9] and [10]). By making the total gravitational potential deeper, self-gravity makes the ring larger in size by $\sim 5 - 20\%$, with larger values corresponding to larger Q_b . Combined with the results of Paper I that showed that the ring position is insensitive to the mass of a central BH (and thus to the number and locations of ILRs), this clearly evidences that the ring position is not determined by the resonant interactions of gas with the underlying gravitational potential but rather by the amount of angular momentum loss at the dust-lane shocks.

Comerón et al. (2010) also presented the sizes of nuclear rings in their sample of barred spiral galaxies. Figure 17b compares their results (star symbols) with our simulation outcomes (squares with errorbars) on the r_{ring}/a - Q_b plane. Both observational and numerical results show that r_{ring}/a becomes smaller with increasing Q_b , indicating that stronger bars can possess smaller rings. For $Q_b \lesssim 0.15$, the agreement between observational and numerical results is quite good. For $Q_b \gtrsim 0.15$, on the other hand, r_{ring}/a in our models corresponds roughly to the upper envelope of the observational results for given Q_b . This is presumably because our numerical models are unmagnetized: inclusion of magnetic fields efficiently removes angular momentum further at dust-lane shocks, which makes the ring size smaller by a factor of ~ 2 when magnetic fields have an equipartition strength with the thermal energy (Kim & Stone 2012). A larger effective sound speed can additionally make the

rings smaller (Paper I).

More recently, Mazzuca et al. (2011) measured the ring radii for a sample of 13 barred/unbarred galaxies that contain star-forming nuclear rings: their results for 8 galaxies whose bar sizes are given in Comerón et al. (2010) are plotted in Figure 17b as triangles. Mazzuca et al. (2011) argued that the ring size is well correlated with the compactness $\mathcal{C} \equiv v_0^2/r_t$, where r_t is the turnover radius of the rotation curve that has the velocity v_0 at the flat part, such that more compact (with smaller turnover radius) galaxies have a smaller ring. In our galaxy models, however, $r_t \sim 1$ kpc and $\mathcal{C} \sim 4 \times 10^4 (\text{km s}^{-1})^2 \text{ kpc}^{-1}$, insensitive to Q_b and \mathcal{R} , while the variation of the ring size with Q_b is about by a factor of $\sim 2-3$. Since the sample galaxies in Mazzuca et al. (2011) also exhibit a positive correlation between \mathcal{C} and Q_b , the negative correlation between \mathcal{C} and r_{ring} in their results may simply be a reflection of a more intrinsic negative correlation between r_{ring} and Q_b . Of course, our current models with a limited range of the parameters cannot address the effects of \mathcal{C} on the ring size.

4. Nuclear Rings: Shape – Not all the rings have a conventional shape similar to x_2 -orbits in our models unless self-gravity is included. In non-self-gravitating models with $f_{\text{bar}} = 0.6$ and $\mathcal{R} \geq 2.0$, the inflowing gas cannot settle on x_2 -orbits since they have too small kinetic energy. The ring material instead takes on an inclined orbit in between x_1 - and x_2 -families. An inclined ring in these models becomes smaller and more eccentric as low angular-momentum gas is added from outside. It loses much of its mass through the inner boundary when its short axis moves close to the center. Due to the bar torque, the inclined ring precesses slowly to align its long axis parallel to the bar major axis, eventually forming an x_1 -type ring. Strong self-gravity of an inclined ring provides additional non-axisymmetric torque that prevents the precession of an inclined ring, leading instead to an x_2 -type ring in self-gravitating models.

When $f_{\text{bar}} \leq 0.3$ or $\mathcal{R} \leq 1.5$, on the other hand, the x_2 -family of closed orbits near the center have sufficiently large kinetic energy that the inflowing gas along the dust lanes can transit easily to one of them in both non-self-gravitating and self-gravitating models. These rings are eccentric with an ellipticity of $\epsilon_{\text{ring}} \sim 0.2-0.3$ insensitive to Q_b , which is within the range of the observed ring ellipticities, $\sim 0-0.4$, reported by Comerón et al. (2010) and Mazzuca et al. (2011). Again, magnetic fields are expected to circularize nuclear rings (Kim & Stone 2012).

5. Nuclear Spirals – Well-defined twin-armed nuclear spirals grow only in models in which the nuclear ring is of the x_2 -type and sufficiently large in size: they would otherwise be destroyed by the ring material on highly eccentric orbits. Even in models with an x_2 -type ring, nuclear spirals are absent if the ring is so small to limit their spatial extent. All nuclear spirals in our models are trailing and logarithmic in shape. While the shapes of dust lanes and nuclear rings do not change much with time after the potential is fully turned on, nuclear spirals are not stationary over the course of the entire evolution. They initially start out as being tightly wound and weak, and then gradually unwind and become stronger until turning into shocks. This unwinding and growth of nuclear spirals appears to be a generic prop-

erty of nonlinear waves that become more nonlinear as they propagate inward (Lee & Goodman 1999). The unwinding rate is lower in self-gravitating models than in non-self-gravitating models. Since nuclear spirals grow and unwind faster as Q_b increases, the probability of having more tightly-wound and weaker spirals is larger for galaxies with a weaker bar torque. This is consistent with the observational results of Peeples & Martini (2006) who found that tightly wound spirals are found primarily in weakly barred galaxies, while loosely wound spirals are more common in strongly barred galaxies (see also Martini et al. 2003a,b). Peeples & Martini (2006) also found that grand-design nuclear spirals in strongly barred galaxies does not extend all the way into the nucleus, which is consistent with our numerical results that show that nuclear spirals cease to exist by turning into shocks, and this happens earlier in higher- Q_b models.

6. Mass Inflow Rates – In our models, the mass inflow rate to through the inner boundary is found to be $\dot{M} \sim 10^{-3} - 10^{-2} M_\odot \text{ yr}^{-1}$ for models with $Q_b \lesssim 0.2$ regardless of the presence of self-gravity. Without self-gravity, models with $Q_b \gtrsim 0.2$ but with an x_2 -type ring still have $\dot{M} < 10^{-2} M_\odot \text{ yr}^{-1}$, since most of the inflowing gas is trapped in the ring. If the inflowing gas moves all the way to a central BH, these values of \dot{M} correspond to the Eddington ratio $\lambda \equiv L_{\text{bol}}/L_{\text{Edd}} = 4.5 \times 10^{-2} (\dot{M}/10^{-2} M_\odot \text{ yr}^{-1}) (M_{\text{BH}}/10^7 M_\odot)^{-1} \sim 10^{-3} - 10^{-2}$ (Paper I), potentially explaining low-luminosity Seyfert 1 AGNs. (e.g., Ho 2008). Here, L_{bol} and L_{Edd} denote the bolometric and Eddington luminosities of an AGN, respectively, and 10% of the mass-to-energy conversion efficiency of the accreted material is assumed. Some of our numerical models exhibit unrealistically large mass inflow rates. Non-self-gravitating models in which the central regions are dominated by the gas on x_1 -orbits are found to have $\dot{M} \gtrsim 1 M_\odot \text{ yr}^{-1}$ and sometimes as large as $\sim 10 M_\odot \text{ yr}^{-1}$ when the ring gas on eccentric orbits is accreted directly to the inner boundary. In self-gravitating models with $Q_b \gtrsim 0.2$, on the other hand, rings are unstable to form high-density clumps with mass $\sim 10^6 - 10^7 M_\odot$. These clumps sometimes plunge into the central hole, causing the mass inflow rate to fluctuate

with large amplitudes.

We finally remark some caveats associated with \dot{M} obtained in our simulations and in interpreting it as a mass accretion rate to a central BH. First, \dot{M} from self-gravitating models are definitely more realistic than that from non-self-gravitating models. Still, Models M60R30G and M60R35G can not be applied to real galaxies since they do not possess well-defined nuclear rings: the bar in these models is perhaps too massive or too elongated, or the Ferrers prolate bar is not a good representation of realistic bars. Second, as mentioned earlier, \dot{M} measured is the rate of gas mass that goes in through the inner boundary. This is likely to be an upper limit to the real accretion rate to the BH since some of the inflowing mass changes its orbit before reaching the BH and can possibly come out of the inner boundary. Third, high-density clumps produced by gravitational instability of nuclear rings would undergo star formation, reducing gas content in the rings. Ensuing feedback would destroy them, so that the accretion of dense clumps in real situations would much less frequent than in our simulations. Fourth, a circumnuclear disk with starburst activities can make the accretion rate to the BH much smaller than \dot{M} (e.g., Davies et al. 2007; Watabe et al. 2008; Kawakatu & Wada 2008). Fifth, while magnetic fields are known to enhance \dot{M} considerably (Kim & Stone 2012), they would suppress or reduce gravitational instability of nuclear rings, which tends to reduce \dot{M} . In order to properly evaluate the mass accretion rates, therefore, it is required to run more realistic models of barred galaxies including star formation, feedback, magnetic fields, and other physical processes that affect gaseous features and gas inflows in the nuclear regions.

We acknowledge helpful and stimulating comments from S. Comerón, J. Knapen, and P. Martini, and a thoughtful report from the referee. We are also grateful to R. Shetty and E. Ostriker for sharing their self-gravity solver based on the Kalnajs method. This work was supported by the National Research Foundation of Korea (NRF) grant funded by the Korean government (MEST), No. 2010-0000712.

APPENDIX

BAR STRENGTH FOR A PROLATE FERRERS BAR

In this Appendix, we provide analytic expressions for the bar strength Q_b and the radius $r(Q_b)$ of the maximum bar torque for a galaxy with an $n = 1$ prolate Ferrer bar, whose density distribution is given by equation (1). The eccentricity of the bar is $e \equiv (1 - b^2/a^2)^{1/2}$. Since the maximum bar torque always occurs inside the bar, it is sufficient to consider the interior (i.e., $g \leq 1$) gravitational potential of the bar.

Following the procedures presented by Pfenniger (1984) for triaxial ellipsoids and by Maciejewski & Sparke (2000) for prolate spheroids, one can show that the interior potential of a Ferrers bar with $n = 1$ at the $z = 0$ plane is given by

$$\Phi_{\text{bar}}(x, y) = -(\pi/2) G a b^2 \rho_{\text{bar}} (W_{00} - 2W_{01}x^2 - 2W_{10}y^2 + W_{02}x^4 + 2W_{11}x^2y^2 + W_{20}y^4), \quad (\text{A1})$$

with the coefficients

$$W_{00} = \frac{1}{ae} \ln \left(\frac{1+e}{1-e} \right) = \frac{I}{a}, \quad (\text{A2})$$

$$W_{10} = \frac{2}{a^3 e^2} \left[\frac{1}{2e} \ln \left(\frac{1+e}{1-e} \right) - 1 \right] = \frac{A_3}{ab^2}, \quad (\text{A3})$$

$$W_{01} = \frac{1}{a^3 e^2} \left[\frac{1}{1-e^2} - \frac{1}{2e} \ln \left(\frac{1+e}{1-e} \right) \right] = \frac{A_1}{ab^2}, \quad (\text{A4})$$

$$W_{11} = (W_{01} - W_{10})/(a^2 e^2), \quad (\text{A5})$$

$$W_{20} = \frac{2}{3} \left(\frac{1}{a^5(1-e^2)} - W_{11} \right), \quad (\text{A6})$$

and

$$W_{02} = \frac{1}{4} \left(\frac{2}{a^5(1-e^2)^2} - W_{11} \right). \quad (\text{A7})$$

Note that I , A_1 , and A_3 in equations (A2) – (A4) are identical to the dimensionless coefficients for the gravitational potential of uniform spheroids tabulated in Table 2.1 of Binney & Tremaine (2008).

The gravitational force in the azimuthal direction due to the $n = 1$ prolate is then given by

$$F_T = -\frac{1}{r} \frac{\partial \Phi_{\text{bar}}}{\partial \phi} = -2\pi G a b^2 \rho_{\text{bar}} x y (C_x x^2 + C_0 + C_y y^2)/r, \quad (\text{A8})$$

where

$$C_x = W_{02} - W_{11}, \quad (\text{A9})$$

$$C_0 = W_{10} - W_{01}, \quad (\text{A10})$$

$$C_y = W_{11} - W_{20}. \quad (\text{A11})$$

It can be easily verified that $C_x, C_y \geq 0$ and $C_0 \leq 0$ for $0 \leq e < 1$. In the limit of $e \rightarrow 0$, $C_x = C_y \rightarrow 2e^2/(7a^5)$, while $C_0 \rightarrow -2e^2/(5a^3)$.

It is straightforward to show that the maximum value of $|F_T|$ is

$$F_{T,\text{max}} = \frac{4\pi G a b^2 \rho_{\text{bar}}}{3^{3/2}} \frac{(-C_0)^{3/2}}{C_x^{1/2} + C_y^{1/2}}, \quad (\text{A12})$$

which occurs at $x^2 = -C_0/(3C_x^{1/2})(C_x^{1/2} + C_y^{1/2})^{-1}$ and $y^2 = -C_0/(3C_y^{1/2})(C_x^{1/2} + C_y^{1/2})^{-1}$.

For galaxies with a constant rotational velocity v_0 , the radial gravitational force is $F_R = v_0^2/r$. Therefore, the bar strength parameter defined in equation (4) becomes

$$Q_b = \frac{(rF_T)_{\text{max}}}{v_0^2} = \frac{\pi G a b^2 \rho_{\text{bar}}}{4v_0^2} \frac{C_0^2}{\sqrt{C_x C_y}}, \quad (\text{A13})$$

which is attained at $x^2 = -C_0/(4C_x)$ and $y^2 = -C_0/(4C_y)$, or at the radius

$$r(Q_b) = \frac{(-C_0)^{1/2}}{2} \left(\frac{1}{C_x} + \frac{1}{C_y} \right)^{1/2}. \quad (\text{A14})$$

Let $M_{\text{tot}}(a) = a v_0^2/G$ denote the total galaxy mass within $r < a$. Assuming that the galaxy mass is dominated by the bulge and the bar inside $r = a$, it then follows that

$$Q_b = \frac{15}{32} \frac{a C_0^2}{\sqrt{C_x C_y}} f_{\text{bar}}. \quad (\text{A15})$$

Figure 1 plots Q_b and $r(Q_b)$ in equations (A15) and (A14) as dotted lines, which is not much different from the true bar strength that does not assume flat rotation.

REFERENCES

- Allard, E. L., Knapen, J. H., Peletier, R. F., & Sarzi, M. 2006, *MNRAS*, 371, 1087
- Ann, H. B., & Thakur, P. 2005, *ApJ*, 620, 197
- Athanassoula, E. 1992a, *MNRAS*, 259, 328
- Athanassoula, E. 1992b, *MNRAS*, 259, 345
- Athanassoula, E., Romero-Gómez, M., & Masdemont, J. J. 2009, *MNRAS*, 394, 67
- Balbus, S. A., & Cowie, L. L. 1985, *ApJ*, 297, 61
- Binney, J., & Tremaine, S. 2008, *Galactic Dynamics*, 2nd ed. (Princeton University Press)
- Block, D. L., Buta, R., Knapen, J. H., Elmegreen, D. M., Elmegreen, B. G., & Puerari, I. 2004, *AJ*, 128, 183
- Buta, R. 1986, *ApJS*, 61, 609
- Buta, R., & Combes, F. 1996, *Fund. Cosmic Phys.*, 17, 95
- Buta, R., Laurikainen, E., Salo, H., Block, D. L., & Knapen, J. H. *AJ*, 132, 1859
- Combes, F. 1996, *Barred Galaxies*, eds. R. Buta, D. A. Crocker, & B. G. Elmegreen, *APS Conference*, 91, 286
- Combes F. 2001, in Aretxaga I., Kunth D., Mújica R., eds, *Advanced Lectures on the Starburst-AGN* (World Scientific: Singapore), p223
- Combes F., & Gerin M. 1985, *A&A*, 150, 327
- Combes, F., & Sanders, R. H. 1981, *A&A*, 96, 164
- Comerón, S., Martínez-Valpuesta, I., Knapen, J. H., Beckman, J. E. 2009, *ApJ*, 706, L256
- Comerón, S., Knapen, J. H., Beckman, J. E., Laurikainen, E., Salo, H., Martínez-Valpuesta, & Buta, R. J. 2010, *MNRAS*, 402, 2462
-) Davies, R. I., et al. 2007, *ApJ*, 671, 1388
- Durbala A., Buta R., Sulentic J. W., Verdes-Montenegro L. 2009, *MNRAS*, 397, 1756
- Englmaier, P., & Gerhard, O. 1997, *MNRAS*, 287, 57
- Ferrers, N. M. 1887, *Q. J. Pure Appl. Math.*, 14, 1
- García-Barreto, J. A., Downes, D., Combes, F., Gerin, M., Magri, C., Carrasco, L., & Cruz-Gonzalez, I. 1991, *A&A*, 244, 257
- Ho, L. C. 2008, *ARA&A*, 46, 475
- Hsieh, P.-Y., Matsushita, S., Liu, G. Ho, P. T. P., Oi, N., & Wu, Y.-L. 2011, *ApJ*, 736, 129
- Kalnajs, A. J. 1971, *ApJ*, 166, 275
- Kawakatu, N., & Wada, K. 2008, *ApJ*, 2008, 681, 73
- Knapen J. H., Beckman J. E., Heller C. H., Shlosman I., de Jong R. S. 1995, *ApJ*, 454, 623
- Knapen, J. H., Pérez-Ramírez, D., & Laine, S. 2002, *MNRAS*, 337, 808
- Kim, W.-T., & Ostriker, E. C. 2002, *ApJ*, 570, 132
- Kim, W.-T., & Ostriker, E. C. 2006, *ApJ*, 646, 213
- Kim, W.-T., Seo, W.-Y., Stone, J. M., Yoon, D., & Teuben, P. J. 2012, *ApJ*, 747, 60 (Paper I)
- Kim, W.-T., & Stone, J. M. 2012, *ApJ*, submitted
- Kulesza-Żydzik, B., Kulpa-Dybeł, K., Otmianowska-Mazur, K., Kowal, G., & Soida, M., 2009, *A&A*, 498, L21
- Kulesza-Żydzik, B., Kulpa-Dybeł, K., Otmianowska-Mazur, K., Soida, M., & Urbanik, M. 2010, *A&A*, 522, A61
- Kulpa-Dybeł, K., Otmianowska-Mazur, K., Kulesza-Żydzik, B., Hanasz, M., Kowal, G., Wółtański, D., & Kowalik, K. 2011, *ApJ*, 733, L18
- Laurikainen, E., & Salo, H. 2002, *MNRAS*, 337, 1118
- Laurikainen, E., Salo, H., Buta, R., Knapen, J. H., Speltinckx, T., & Block, D. 2006, *AJ*, 132, 2634
- Laurikainen, E., Salo, H., Buta, R., & Vasylyev, S. 2004, *MNRAS*, 355, 1251
- Lee, E., & Goodman, J. 1999, *MNRAS*, 308, 984
- Lin, L.-H., Yuan, C., & Buta, R. 2008, *ApJ*, 684, 1048
- Maciejewski, W., & Sparke, L. S. 2000, *MNRAS*, 313, 745
- Maciejewski, W., Teuben, P. J., Sparke, L. S., & Stone, J. M. 2002, *MNRAS*, 329, 502
- Maciejewski, W. 2004a, *MNRAS*, 354, 883
- Maciejewski, W. 2004b, *MNRAS*, 354, 892
- Martini, P., Regan, M. R., Mulchaey, J. S., & Pogge, R. W. 2003a, *ApJS*, 146, 353
- Martini, P., Regan, M. R., Mulchaey, J. S., & Pogge, R. W. 2003b, *ApJ*, 589, 774
- Martínez-Valpuesta, I., Shlosman, I., & Heller, C. 2006, *ApJ*, 637, 214
- Mazzuca, L. M., Knapen, J. H., Veilleux, S., & Regan, M. W. 2008, *ApJ*, 174, 337
- Mazzuca, L. M., Swaters, R. A., Knapen, J. H., & Veilleux, S. 2011, *ApJ*, 739, 104
- Patsis, P. A., & Athanassoula, E. 2000, *A&A*, 358, 45
- Pease F. G. 1917, *ApJ*, 46, 24
- Peebles, M. S., & Martini, P. 2006, *ApJ*, 652, 1097
- Pfenniger, D. 1984, *A&A*, 134, 373
- Piner, B. G., Stone, J. M., & Teuben, P. J. 1995, *ApJ*, 449, 508
- Prendergast, K. H. 1962, in *Distribution and Motion of ISM in Galaxies*, ed. L. Woltjer (New York: Benjamin)
- Prieto, M. A., Maciejewski, W., & Reunanen, J. 2005, *AJ*, 130, 1472
- Regan, M. W., & Teuben, P. J. 2003, *ApJ*, 582, 723
- Regan, M. W., & Teuben, P. J. 2004, *ApJ*, 600, 595
- Roberts, W., Huntley, M., & Van Albada, G. D. 1979, *ApJ*, 233, 67
- Sandage, A. 1961, *The Hubble Atlas of Galaxies* (Washington, DC: Carnegie Institution of Washington)
- Sakamoto, K., Okumura, S. K., Ishizuki, S., Scoville, N. Z. 1999, *ApJ*, 525, 691
- Sanders, R. H., & Huntley, J. M. 1976, *ApJ*, 209, 53
- Sarzi, M., Allard, E. L., Knapen, J. H., & Mazzuca, L. M. 2007, *MNRAS*, 380, 949
- Sheth, K., Vogel, S. N., Regan, M. W. et al. 2005, *ApJ*, 632, 217
- Shetty, R., & Ostriker, E. C. 2008, *ApJ*, 684, 978
- Shlosman, I., Begelman, M. C., & Frank, J. 1990, *Nature*, 345, 679
- Thakur, P., Ann, H. B., & Jiang, I. 2009, *ApJ*, 693, 586
- Truelove, J. K., Klein, R. I., McKee, C. F., Holliman, J. H., II, Howell, L. H., & Greenough, J. A. 1997, *ApJ*, 489, L179
- Truelove, J. K., Klein, R. I., McKee, C. F., Holliman, J. H., II, Howell, L. H., Greenough, J. A., & Woods, D. T. 1998, *ApJ*, 495, 821
- van Albada, G. D., & Roberts, W. W. 1981, *ApJ*, 246, 740
- Wada, K., & Koda, J. 2004, *MNRAS*, 349, 270
- Watabe, Y., Kawakatu, N., & Imanishi, M. 2008, *ApJ*, 677, 895